

Field Testing of a Stochastic Planner for ASV Navigation Using Satellite Images

Philip (Yizhou) Huang*
 Department of Computer Science
 University of Toronto
 Toronto, Canada
 phuang@cs.toronto.edu

Tony (Qiao) Wang
 Division of Engineering Science
 University of Toronto
 Toronto, Canada
 tonyivt.wang@mail.utoronto.ca

Florian Shkurti
 Department of Computer Science
 University of Toronto
 Toronto, Canada
 florian@cs.toronto.edu

Timothy D. Barfoot
 Institute for Aerospace Studies
 University of Toronto
 Toronto, Canada
 tim.barfoot@utoronto.ca

Abstract

We introduce a multi-sensor navigation system for autonomous surface vessels (ASV) intended for water-quality monitoring in freshwater lakes. Our mission planner uses satellite imagery as a prior map, formulating offline a mission-level policy for global navigation of the ASV and enabling autonomous online execution via local perception and local planning modules. A significant challenge is posed by the inconsistencies in traversability estimation between satellite images and real lakes, due to environmental effects such as wind, aquatic vegetation, shallow waters, and fluctuating water levels. Hence, we specifically modelled these traversability uncertainties as stochastic edges in a graph and optimized for a mission-level policy that minimizes the expected total travel distance. To execute the policy, we propose a modern local planner architecture that processes sensor inputs and plans paths to execute the high-level policy under uncertain traversability conditions. Our system was tested on three km-scale missions on a Northern Ontario lake, demonstrating that our GPS-, vision-, and sonar-enabled ASV system can effectively execute the mission-level policy and disambiguate the traversability of stochastic edges. Finally, we provide insights gained from practical field experience and offer several future directions to enhance the overall reliability of ASV navigation systems.

1 Introduction

Autonomous Surface Vessels (ASVs) have seen increasing attention as a technology to monitor rivers, lakes, coasts, and oceans in recent years (Ang et al., 2022; Cao et al., 2020; Dash et al., 2021; Dunbabin & Marques, 2012; Ferri et al., 2015; Madeo et al., 2020; MahmoudZadeh et al., 2022; Odetti et al., 2020). A fundamental challenge to the wide adoption of ASVs is the ability to navigate safely and autonomously in uncertain environments, especially for long durations. For example, many existing ASV systems require the user to precompute a waypoint sequence. The robot then visits these target locations on a map and attempts to

*Corresponding Author



(a) Strong wind



(b) Extruding logs



(c) Shallow water



(d) Aquatic plants

Figure 1: Real-world challenges that motivate the use of stochastic edges in our planning setup.

execute the path online (Tang et al., 2020; Vasilj et al., 2017). However, disturbances such as strong winds, waves, unseen obstacles, aquatic plants that may or may not be traversable, and even simply changing visual appearances in a water environment are challenging for ASV navigation (Fig. 1). Many potential failures in robot perception and control systems may also undermine the mission’s overall success.

Our long-term goal is to use an ASV to monitor lake environments and collect water samples for scientists. A requirement for achieving this, and the primary focus of this paper, is to ensure robust global and safe local navigation. To enhance the robustness of the overall system, we identify waterways that are prone to local blockage as stochastic edges and plan mission-level policies on our high-level map. Uncertainties that arise during policy execution are handled by the local planner. One planning framework that is suitable for modelling uncertain paths is the Canadian Traveller Problem (CTP) (Papadimitriou & Yannakakis, 1991), a variant of the shortest-path planning problem for an uncertain road network. The most significant feature in a CTP graph is the stochastic edge, which has a probability of being blocked. The state of any stochastic edge can be disambiguated by visiting the edge. Once the state has been visited and classified as traversable or not, it remains the same.

In our prior work (Y. Huang et al., 2023), we proposed a navigation framework — the Partial Covering Canadian Traveller Problem (PCCTP) — to solve a mission-planning problem in an uncertain environment. The framework used a stochastic graph derived from coarse satellite images to plan an adaptive policy that visits all reachable target locations. Stochasticity in the graph represents possible events where a water passage between two points is blocked due to changing water levels, strong wind, and other unmapped obstacles. The optimal policy is computed offline with a best-first tree-search algorithm. We evaluated our solution method on 1052 Canadian lakes selected from the *CanVec Series Ontario* dataset (Natural Resources Canada, 2019) and showed it can reduce the total distance to visit all targets and return.

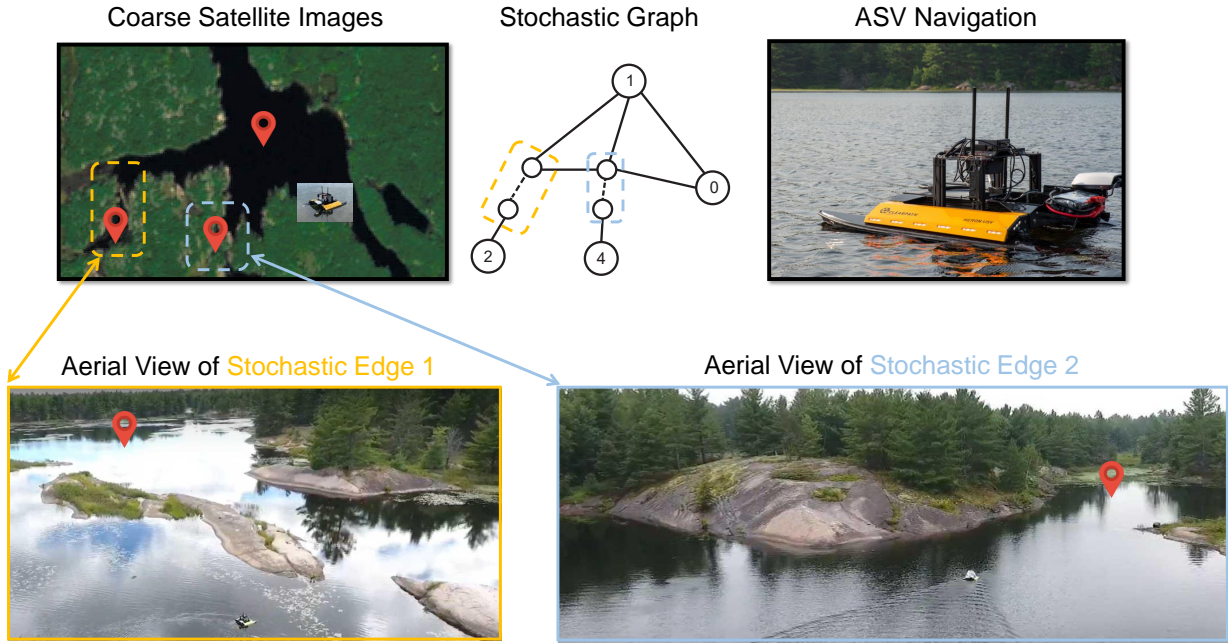


Figure 2: A high-level overview of our navigation framework for water sampling. Given a set of user-selected target locations (red icons), our algorithm identifies stochastic edges from coarse satellite images and plans a mission-level policy for ASV navigation. Aerial views of two stochastic edges from real-world experiments are shown here.

This article extends our previous work as described by Y. Huang et al. (2023) in two ways. First, we made significant improvements to our local planner responsible for tracking the global path and handling any locally occurring uncertainties such as obstacles. Our ASV system estimates the waterline using a learned network and a stereo camera and detects underwater obstacles using a mechanically scanning sonar. We fuse both sensors into an occupancy grid map, facilitating a sampling-based local motion planner to compute a pathway to track the global path while avoiding local obstacles. As in our previous research, we use a timer to distinguish stochastic edges and select appropriate policy branches based on the traversability assessment of the stochastic edges. Secondly, we have validated the overall system on three distinct missions, two of which are new. Our field trials show that our ASV reliably and autonomously executes precomputed policies from the mission planner under varying operating conditions and amid unmapped obstacles, even when the local planner does not perfectly map the local environment or optimally steer the ASV. We have also tested the local planner through an ablation study to identify bottlenecks in localization, mapping, and sensor fusion in the field. Our lessons learned from our field tests are detailed, and we believe this work will serve as a beneficial reference for any future ASV systems developed for environmental monitoring.

2 Related Works

Autonomous ASV navigation for environmental monitoring requires domain knowledge from multiple fields, such as perception, planning, and overall systems engineering. In this section, we present a brief survey of all these related fields and discuss the relationship to our methods and any remaining challenges.

Satellite Imagery Mapping First, mission planning in robotics often requires a global, high-level map of the operating environment. Remote sensing is a popular technique to build maps and monitor changes in water bodies around the world because of its efficiency (C. Huang et al., 2018; X. Yang et al., 2017). The

JRC Global Surface Water dataset (Pekel et al., 2016) maps changes in water coverage from 1984 to 2015 at a 30 m by 30 m resolution, produced using *Landsat* satellite imagery. Since water has a lower reflectance in the infrared channel, an effective method is to calculate water indices, such as Normalized Difference Water Index (NDWI) (McFeeters, 1996) or MNDWI (Xu, 2006), from two or more optical bands (e.g., green and near-infrared). However, extracting water data using a threshold in water indices can be nontrivial due to variations introduced by clouds, seasonal changes, and sensor-related issues. To address this, Li and Sheng (2012) and Feyisa et al. (2014) have developed techniques to select water-extraction thresholds adaptively. Our approach aggregates water indices from historical satellite images to estimate probabilities of water coverage (see Sec. 3.3). Overall, we argue that it is beneficial to build stochastic models of surface water bodies due to their dynamic nature and imperfect knowledge derived from satellite images.

Global Mission Planning The other significant pillar of building an ASV navigation system is mission planning. First formulated in the 1930s, the Travelling Salesman Problem (TSP) (Laporte, 1992) studies how to find the shortest-path in a graph that visits every node once and returns to the starting node. Modern TSP solvers such as the *Google OR-tools* (Perron & Furnon, 2023) can produce high-quality approximate solutions for graphs with about 20 nodes in a fraction of a second. Other variants have also been studied in the optimization community, such as the Travelling Repairman Problem (Afrati et al., 1986) that minimizes the total amount of time each node waits before the repairman arrives, and the Vehicle Routing Problem (Toth & Vigo, 2002) for multiple vehicles. In many cases, the problem graphs are built from real-world road networks, and the edges are assumed to be always traversable. In CTP (Papadimitriou & Yannakakis, 1991), however, edges can be blocked with some probability. The goal is to compute a policy that has the shortest expected path to travel from a start node to a single goal node. CTP can also be formulated as a Markov Decision Process (Bellman, 1957) and solved optimally with dynamic programming (Polychronopoulos et al., n.d.) or heuristic search (Aksakalli et al., 2016). The robotics community has also studied ways in which the CTP framework can be best used in path planning (Ferguson et al., 2004; Guo & Barfoot, 2019). Our problem setting, the Partial Covering Canadian Traveller Problem (PCCTP), lies at the intersection of TSP and CTP, where the goal is to visit a partial set of nodes on a graph with stochastic edges. A similar formulation, known as the Covering Canadian Traveller Problem (CCTP) (Liao & Huang, 2014), presents a heuristic, online algorithm named Cyclic Routing (CR) to visit every node in a complete n -node graph with at most $n - 2$ stochastic edges. A key distinction between CCTP and our setting is that CCTP assumes all nodes are reachable, whereas in PCCTP, the robot may give up on unreachable nodes located behind an untraversable edge.

ASV Systems In recent years, more ASV systems and algorithms for making autonomous decisions to monitor environments have been built. Schiaretti et al. (2017) classify the autonomy level for ASVs into 10 levels based on control systems, decision making, and exception handling. Many works consider the mechanical, electrical, and control subsystems of their ASV designs (Ang et al., 2022; Ferri et al., 2015; Madeo et al., 2020). Dash et al. (2021) validated the use and accuracy of deploying ASVs for water-quality modelling by comparing the data collected from ASVs against independent sensors. Two examples of vertically integrated autonomous water-quality monitoring systems using ASVs are presented by H.-C. Chang et al. (2021) and Cao et al. (2020). In contrast, our main contribution is a robust mission-planning framework that is complementary to existing designs of ASV systems. Finally, informative path planning is another orthogonal area where the robot relies on a probabilistic model to identify targets that maximize information gain; Bai et al. (2021) reviews this topic.

Local Motion Planning Path planning for navigation and obstacle avoidance is a comprehensive field that has been extensively studied (Sanchez-Ibanez et al., 2021). The primary purpose of the local planner in this project is to successfully identify and follow a safe path that tracks the global path while averting locally detected obstacles in real-time. Sampling-based motion planners such as RRT* (Karaman & Frazzoli, 2011) and BIT* (Gammell et al., 2015) are favourable, owing to their probabilistically complete nature and proven asymptotic optimality given the right heuristics. Our local motion planner is based on Sehn et al. (2023), a variant of the sampling-based planner designed to follow a reference path. Using a new edge-cost metric and planning in the curvilinear space, their proposed planner can incrementally update its path to avoid new or moving obstacles without replanning from the beginning while minimizing deviation to the global reference

path. Search-based algorithms, such as D* lite (Koenig & Likhachev, 2002) and Field D* (Ferguson & Stentz, 2007), commonly used in mobile robots and autonomous vehicles, operate on a discretized 2D grid and employ a heuristic to progressively locate a path from the robot’s present location to the intended destination. Subsequently, the optimal solution from the path planning is submitted to a low-level controller tasked with calculating the necessary velocities or thrusts in mobile robotics systems. Parallel to the planning and control framework, other models such as direct tracking with a constrained model-predictive controller (Ji et al., 2016) and training policies for path tracking through reinforcement learning (Shan et al., 2020) have emerged as new areas of research in recent years.

Perception Lastly, our navigation framework requires local perception modules to clarify uncertainties in our map and avoid obstacles. Vision-based obstacle detection and waterline segmentation have also received renewed attention in the marine robotics community. Recent contributions have largely focused on detecting or segmenting obstacles from RGB images using neural networks (Lee et al., 2018; Qiao et al., 2022; Steccanella et al., 2020; Teršek et al., 2023; J. Yang et al., 2019). A substantial amount of research has been dedicated to identifying waterlines (Steccanella et al., 2020; Steccanella et al., 2019; Yin et al., 2022; Zhou et al., 2022) since knowing the whereabouts of navigable waterways can often be sufficient for navigation. Several annotated datasets collected in different water environments, such as inland waterways (Cheng et al., 2021) and coastal waters (Bovcon et al., 2019, 2021) have been published by researchers. Foundational models for image segmentation, such as ‘Segment Anything’ (Kirillov et al., 2023), have also gathered increasing attention due to their incredible zero-shot generalization ability and are being used in tracking (Maalouf et al., 2023) or remote sensing tasks (Chen et al., 2023). Sonar is another popular sensor that measures distance and detects objects on or under water surfaces using sound waves. Heidarsson and Sukhatme (2011a) pioneered the use of a mechanical scanning sonar for ASV obstacle detection and avoidance and demonstrated that obstacles generated from sonar could serve as labels for aerial images (Heidarsson & Sukhatme, 2011b). Karoui et al. (2015) focused on detecting and tracking sea-surface objects and wakes from a forward-looking sonar image. Occupancy-grid mapping, a classic probabilistic technique for mapping the local environment, was used to fuse measurements from sonars and stereo cameras on a mobile ground robot (Elfes, 1989). For our perception pipeline, we combine the latest advances in computer vision, large datasets from the field, and traditional filtering techniques to make the system robust in real-world operating conditions. Despite advances, accurate sensor fusion of above-water stereo cameras and underwater sonar for precise mapping on an ASV remains a formidable research challenge.

3 Global Mission Planner

In this section, we will describe the mathematical formulation of the planning problem and present a detailed breakdown of our algorithm.

3.1 The Problem Formulation

We are interested in planning on a graph representation of a lake where parts of the water are stochastic (i.e., uncertain traversability). Constructing such a graph using all pixels of satellite images is impractical since images are very high-dimensional. Thus, we extend previous works from CTP (Guo & Barfoot, 2019; Liao & Huang, 2014; Papadimitriou & Yannakakis, 1991) and distill satellite images into a high-level graph G where some stochastic edges e may be untraversable with probability p . The state of a stochastic edge can be disambiguated only when the robot traverses the edge in question. The robot begins at the starting node s and is tasked to visit all reachable targets J specified by the user (e.g., scientists) before returning to the starting node. If some target nodes are unreachable because some stochastic edges block them from the starting node, the robot may give up on these sampling targets. We call this problem the Partial Covering Canadian Traveller Problem (PCCTP). Fig. 3 is a simplified graph representation of a lake with two stochastic edges. The state of the robot is defined as a collection of the following: a list of target nodes that it has visited, the current node it is at, and its knowledge about the stochastic edges. A policy sets the next node to visit, given the current state of the robot. The objective is to find the optimal policy π^* that

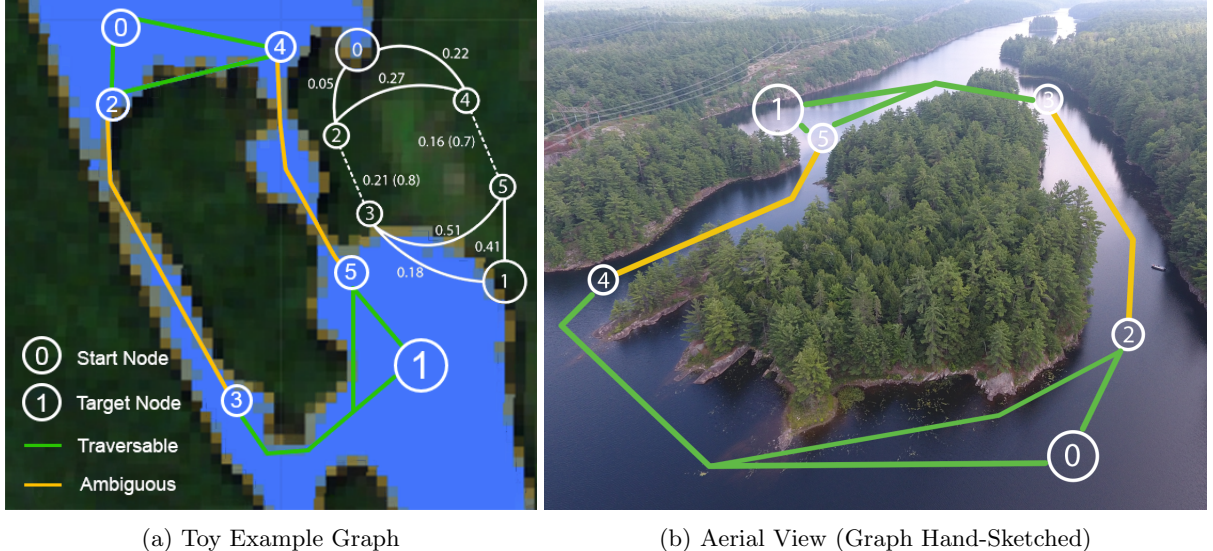


Figure 3: A toy example graph shown on the water mask generated from *Sentinel-2* satellite images, with the corresponding graph on an aerial view image shown on the right. The planned paths between nodes are simplified for ease of understanding. The number beside each edge of the high-level graph is the path length in km, and the number in brackets is the blocking probability, which is computed using the probability of water coverage in each pixel (represented by its shade of orange) on the path. Note that traversable and ambiguous edges are the state before any action.

minimizes the expected cost to cover all reachable targets. In the example problem (Fig. 3), the robot can either disambiguate the left or right stochastic edge to reach the sampling location. Formally, we define the following terms:

- $G = (V, E)$ is an undirected graph.
- $c : E \rightarrow \mathbb{R}_{\geq 0}$ is the cost function for an edge, which is the length of the shortest waterway between two points.
- $p : E \rightarrow [0, 1]$ is the blocking probability function. An edge with 0 blocking probability is deterministic; otherwise, it is stochastic.
- k is the number of stochastic edges.
- $s \in V$ is the start and return node.
- $J \subseteq V$ is the subset of target nodes to visit. There are $|J| \leq |V|$ goal nodes.
- $I = \{A, T, U\}^k$ is an information vector that represents the robot's knowledge of the status of all k stochastic edges. A, T, and U stand for ambiguous, traversable, and untraversable, respectively.
- $S \subseteq J$ is the subset of target nodes that the robot has visited.
- a is the current node the robot is at.
- $x = (a, S, I)$ is the state of the robot. a is the current node, S is the set of visited targets, and I is the current information vector.
- π^* is the optimal policy that minimizes the cost $\mathbb{E}_{w \sim p(w)} [\phi(\pi)]$, where ϕ is cost functional of the policy π and w is a possible world of stochastic graph, where each stochastic edge is assigned a traversability state.

3.2 Exactly Solving PCCTP with AO*

We extend the AO* search algorithm (Aksakalli et al., 2016) used in CTP to find exact solutions to our problem. AO* is a heuristic, best-first search algorithm that iteratively builds an AO tree to explore the state space until the optimal solution is found. In this section, we will first explain how to use an AO tree to represent a PCCTP instance, then break down how to use AO* to construct the AO tree containing the optimal policy.

AO Tree Representation of PCCTP The construction of the AO tree is a mapping of all possible actions the robot can take and all possible disambiguation outcomes at every stochastic edge. Following Aksakalli et al. (2016), an AO tree is a rooted tree $T = (N, A)$ with two types of nodes and arcs. A node $n \in N$ is either an OR node or an AND node; hence the node set N can be partitioned into the set of OR nodes N_O and the set of AND nodes N_A . Each arc in A represents either an action or a disambiguation outcome and is not the same as G 's edges ($A \neq E$). For all $n \in N$, a function $c : A \rightarrow \mathbb{R}_{\geq 0}$ assigns the cost to each arc. Also, for all $n \in N_A$, a function $p : A \rightarrow [0, 1]$ assigns a probability to each arc. A function $f : N \rightarrow \mathbb{R}_{\geq 0}$ is the cost-to-go function if it satisfies the following conditions:

- if $n \in N_A$, $f(n) = \sum_{n' \in N(n)} [p(n, n') \times (f(n') + c(n, n'))]$,
- if $n \in N_O$, $f(n) = \min_{n' \in N(n)} [f(n') + c(n, n')]$,
- if $n \in N$ is a leaf node, $f(n) = 0$.

Now, we can map each node and edge such that the AO tree represents a PCCTP instance. Specifically, each node n is assigned a label $(n.a, n.S, n.I)$ that represents the state of the robot. $n.a$ is the current node, $n.S$ is the set of visited targets, and $n.I$ is the information vector containing the current knowledge of the stochastic edges. The root node r is an OR node with the label $(s, \emptyset, AA...A)$, representing the starting state of the robot. An outgoing arc from an OR node n to its successor n' represents an action, which can be either visiting the remaining targets and returning to the start or going to the endpoint of an ambiguous edge via some target nodes along the way. An AND node corresponds to the disambiguation event of a stochastic edge, so it has two successors describing both possible outcomes. Each succeeding node of an OR node is either an AND node or a leaf node. A leaf node means the robot has visited all reachable target nodes and has returned to the start node. Each arc (n, n') is assigned a cost c , which is the length of travelling from node $n.a$ to node $n'.a$ while visiting the subset of newly visited targets $n'.S \setminus n.S$ along the way. For all outgoing arcs of an AND node, the function p assigns the traversability probability for the stochastic edge. The cost of disambiguating that edge is its length.

Once the complete AO tree is constructed, the optimal policy is the collection of nodes and arcs included in the calculation of the cost-to-go from the root of the tree, and the optimal expected cost is $f(r)$. For example, the optimal action at an OR node n is the arc (n, n') that minimizes the cost-to-go from n , while the next action at an AND node depends on the disambiguation outcome. However, constructing the full AO tree from scratch is not practical since the space complexity is exponential with respect to the number of stochastic edges. Instead, we use the heuristic-based AO* algorithm, explained below.

PCCTP-AO* Algorithm Our PCCTP-AO* algorithm (Algorithm 1 and 2) is largely based on the AO* algorithm (C. L. Chang & Slagle, 1971; Martelli & Montanari, 1978). AO* utilizes an admissible heuristic $h : N \rightarrow \mathbb{R}_{\geq 0}$ that underestimates the cost-to-go f to build the AO tree incrementally from the root node until the optimal policy is found. The algorithm expands the most promising node in the current AO tree based on a heuristic and backpropagates its parent's cost recursively to the root. This expansion-backpropagation process is repeated until the AO tree includes the optimal policy.

One key difference between AO* and PCCTP-AO* is that the reachability of a target node may depend on the traversability of a set of critical stochastic edges connecting the target to the root. If a target $j \in J$

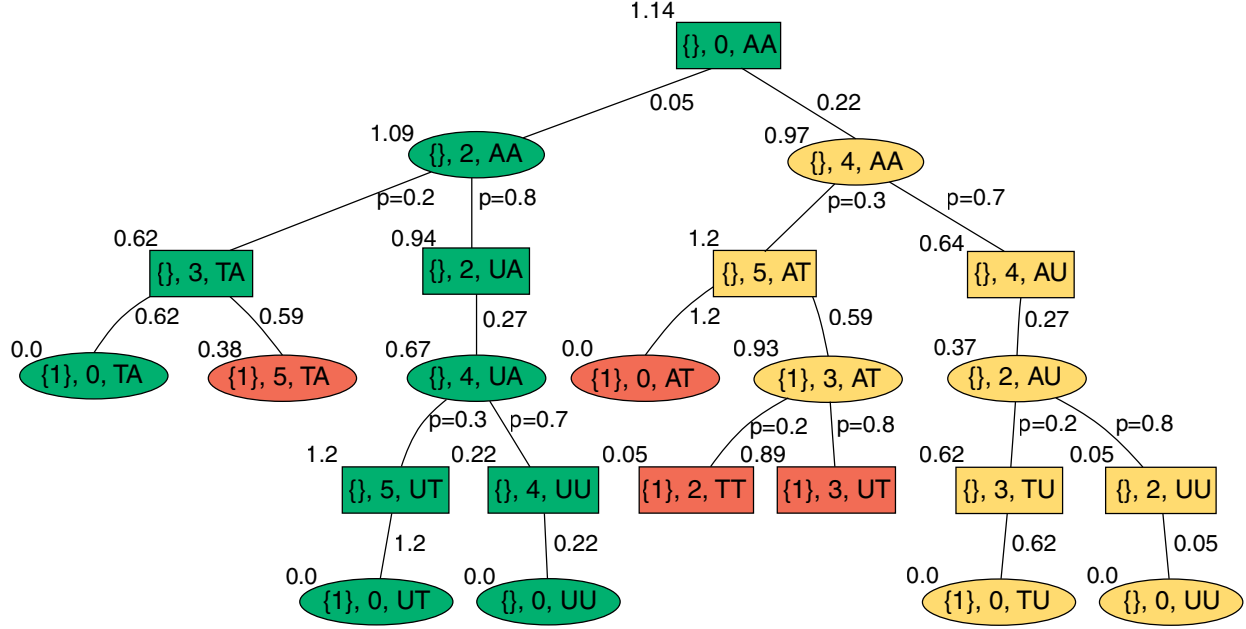


Figure 4: The final AO tree after running PCCTP-AO* on the example in Fig. 3. The label inside each node is the current state of the robot. OR nodes are rectangles, and AND nodes are ellipses. Nodes that are part of the final policy are green, extra expanded nodes are yellow, and leaf nodes terminated early are red. Some red nodes that are terminated early are left out in this figure for simplicity.

is disconnected from the current node a when all the stochastic edges from a particular set are blocked, then this set of edges is critical. For example, the two stochastic edges in the top-right graph of Fig. 3 are critical because target node 1 would be unreachable if both edges were blocked. Thus, a simple heuristic that assumes all ambiguous edges are traversable may overestimate the cost-to-go if skipping unreachable targets reduces the overall cost.

Alternatively, we can construct the following relaxed problem to calculate the heuristic. If a stochastic edge is not critical to any target, we still assume it is traversable. Otherwise, we remove the potentially unreachable target for the robot and instead disambiguate one of the critical edges of the removed target. The heuristic is the cost of the best plan that covers all definitively reachable targets and disambiguates one of the critical stochastic edges. For example, consider computing the heuristic at starting node 0 in Fig. 5. The goal is to visit both nodes 1 and 2 if they are reachable. Node 1 is always reachable; hence we assume it is traversable in the relaxed problem. Node 2 may be unreachable, so we remove the stochastic edge $(4, 2)$ and ask the boat to visit Node 4 instead in the relaxed problem. This heuristic is always admissible because the path to disambiguate a critical edge is always a subset of the eventual policy. We can compute this by constructing an equivalent generalized travelling salesman problem (Noon & Bean, 1993) and solve it with any optimal TSP solver.

Fig. 4 shows the result of applying PCCTP-AO* to the example problem in Fig. 3. The returned policy (coloured in green nodes) tries to disambiguate the closer stochastic edge $(2, 3)$ to reach target node 1. Note that the AO* algorithm stops expanding as soon as the lower bound of the cost of the right branch exceeds that of the left branch. This guarantees the left branch has a lower cost and, thus, is optimal.

3.3 Estimating Stochastic Graphs From Satellite Imagery

We will now explain our procedure to estimate the high-level stochastic graph from satellite images.

Water Masking Our first step is to build a water mask of a water area across a specific period (e.g.,

Algorithm 1 The PCCTP-AO* Algorithm

Require: Graph $G(V, E)$, cost function c , heuristic h , blocking probability p , target set J , k stochastic nodes, start node s

- 1: $n.a = s$, $n.S = \emptyset$, $n.I = \{A\}^k$
- 2: $f(n) = h(n)$; $n.type = \text{OR}$; $T.root = n$
- 3: **while** $T.root.status \neq \text{solved}$ **do**
- 4: $n = \text{SELECTNODE}(T.root)$
- 5: **for** $n' \in \text{EXPAND}(n, T)$ **do**
- 6: $f(n') = h(n')$
- 7: **if** $\text{REACHABLESET}(J, n'.I) \subseteq n'.S$ **then**
- 8: $n'.status = \text{solved}$
- 9: **end if**
- 10: **end for**
- 11: $\text{BACKPROP}(n, T)$
- 12: **end while**
- 13: **if** $T.root.f == \text{inf}$ **then return** No Solution
- 14: **end if**
- 15: **return** T
- 16: **function** $\text{BACKPROP}(n, T)$ \triangleright Update the cost of the parent of n recursively until the root. Same as in Guo and Barfoot (2019).
- 17: **while** $n \neq T.root$ **do**
- 18: **if** $n.type == \text{OR}$ **then**
- 19: $n^* = \text{argmin}_{n' \in N(n)} [f(n') + c(n, n')]$
- 20: $f(n) = f(n^*) + c(n, n^*)$
- 21: **if** $n^*.status == \text{solved}$ **then** $n.status = \text{solved}$
- 22: **end if**
- 23: **end if**
- 24: **if** $n.type == \text{AND}$ **then**
- 25: $f(n) = \sum_{n' \in N(n)} [p(n, n') \times (f(n') + c(n, n'))]$
- 26: **if** $n'.status == \text{solved} \ \forall n' \in N(n)$ **then**
- 27: $n.status = \text{solved}$
- 28: **end if**
- 29: **end if**
- 30: $n = n.parent$
- 31: **end while**
- 32: **end function**

30 days). We use the *Sentinel-2* Level 2A dataset (Drusch et al., 2012), which has provided multispectral images at 10 m by 10 m resolution since 2017. Each geographical location is revisited every five days by a satellite. We then select all satellite images in the target spatiotemporal window and filter out the cloudy images using the provided cloud masks. For each image, we calculate the Normalized Difference Water Index (NDWI) (McFeeters, 1996) for every pixel using green and near-infrared bands. However, the distribution of NDWI values varies significantly across different images over time. Thus, we separate water from land in each image and aggregate the indices over time. We then fit a bimodal Gaussian Mixture Model on the histogram of NDWIs to separate water pixels from non-water ones for each image. We average all water masks over time to calculate the probabilistic water mask at the target spatiotemporal window. Each pixel on the final mask represents the probability of water coverage on this 10 m by 10 m area. If a pixel may or may not have water, we call it a stochastic pixel. Finally, we identify the boundary of all deterministic water pixels. Fig. 6 shows an overview of these steps.

Stochastic Edge Detection: Pinch Points We can now identify those stochastic water paths (i.e., narrow straits, pinch points (Ferguson et al., 2004)) that are useful for navigation. A pinch point is a sequence of stochastic water pixels connecting two parts of topologically far (or distinct) but metrically close water

Algorithm 2 Algorithm for AO* Expansion

```

1: function SELECTNODE( $n$ )     $\triangleright$  Find the most promising subtree recursively until reaching a leaf node.
2:   if  $N(n)$  == empty then return  $n$ 
3:   end if
4:    $\text{best} = \text{argmin}_{n' \in N(n)} [f(n') + c(n, n')]$ 
5:   return SELECTNODE(best)
6: end function
7: function EXPAND( $n, T$ )     $\triangleright$  Find the set of succeeding nodes for node  $n$  and add them to the tree  $T$ .
8:    $N(n) = []$ 
9:   if  $n.\text{type} == \text{OR}$  then
10:     $J^R = \text{REACHABLESET}(J, n.I)$ 
11:     $q = \text{Queue}(); q.append((n.S, n.a))$ 
12:     $\text{cost} = \text{Dictionary}\{(n.S, n.a) : 0\}$ 
13:    while  $q$  is not empty do                                 $\triangleright$  Search all paths that end up at an ambiguous edge
14:       $n = q.pop()$ 
15:       $A = \{a \mid \text{HASAMBIGUOUSEDGE}(a) \ \forall a \in V\}$ 
16:      for  $a' \in (J^R \cup A) \setminus n.S$  do
17:         $S' = (n.S \cup \text{PATH}(n.a, a')) \cap J^R$ 
18:         $c' = \text{cost}[(n.S, n.a)] + c(n.a, a')$ 
19:        if  $(S', a')$  not in  $\text{cost}$  or  $\text{cost}[(S', a')] > c'$  then
20:           $\text{cost}[(S', a')] = c'$                                  $\triangleright$  Update the best path and best cost
21:           $q.append((S', a'))$ 
22:        end if
23:      end for
24:    end while
25:     $\text{costf} = \text{Dictionary}\{ \}$                                  $\triangleright$  Find the best route to visit all targets and return to start
26:    for  $(S, a) \in \text{costs}$  do
27:       $n' = (S, a, n.I); N(n).append(n')$                        $\triangleright$  Add to set of succeeding nodes
28:      if  $S \subseteq J^R$  then
29:         $\text{costf}[(S, a)] = \text{cost}[(S, a)] + c(a, s)$ 
30:      end if
31:    end for
32:     $S^f, a^f = \text{argmin}_{S^f, a^f} \text{costf}[(S, a)]$ 
33:     $n^f = (S^f, a^f, n.I); N(n).append(n^f)$                    $\triangleright$  Add to set of succeeding nodes
34:  end if
35:  if  $n.\text{type} == \text{AND}$  then
36:    for  $e \in \text{AMBIGUOUSEDGE}(n.a)$  do                       $\triangleright$  Expand the disambiguation of ambiguous edges
37:       $n^T.I = \text{UNBLOCK}(n^T.I, e); N(n).append(n^T)$ 
38:       $n^U.I = \text{BLOCK}(n^U.I, e); N(n).append(n^U)$ 
39:    end for
40:  end if
41:  return  $N(n)$ 
42: end function

```

areas. Essentially, this edge is a shortcut connecting two points on the water boundary that are otherwise far away or disconnected. To find all such edges, we iterate over all boundary pixels, test each shortest stochastic water path to nearby boundary pixels, and include those stochastic paths that are shortcuts. The blocking probability of a stochastic edge is one minus the minimum water probability along the path. Since this process will produce many similar stochastic edges around the same narrow passage, we run DBSCAN (Ester et al., 1996) and only choose the shortest stochastic edge within each cluster.

Stochastic Edge Detection: Windy Edges The second type of stochastic edges are those with strong wind. In practice, when an ASV travels on a path far away from the shore, there is a higher chance of

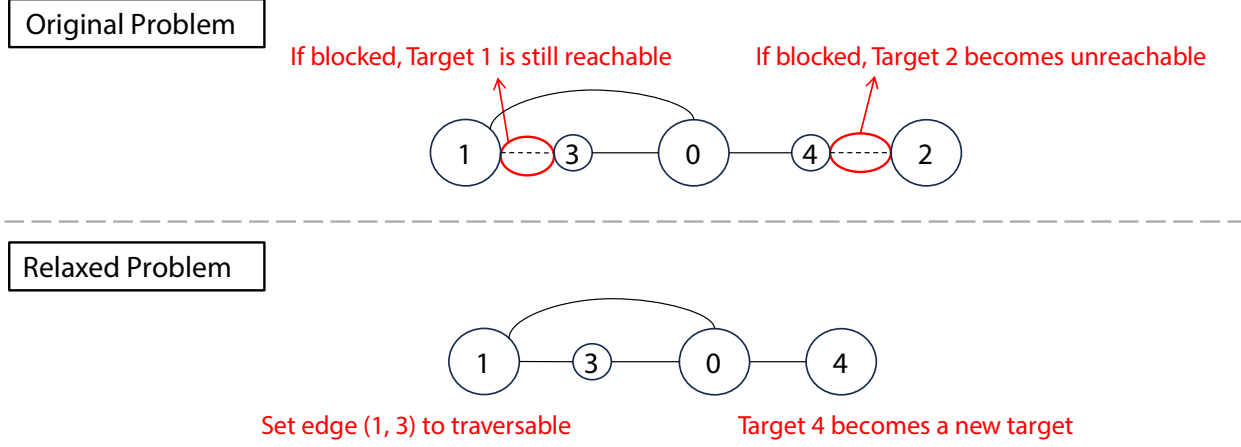


Figure 5: Example of how we relax the original problem graph to calculate the heuristic $h(n)$. At a high level, we construct a relaxed problem by removing all stochastic edges and unreachable nodes from the original graph. Then, the heuristic of the original problem is the cost of the relaxed problem and is always admissible.

running into a strong headwind or wave, making the path difficult to traverse. We define an edge as a windy edge if it is 200 m away from the water boundary at some point and assign a small probability for the event where the wind blocks the edge.

Path Generation The next step is to construct the geo-tagged path and calculate all edge costs in the high-level graph. The nodes in the high-level graph are composed of all sampling targets, endpoints of stochastic edges, and the starting node. We run A* (Hart et al., 1968) on the deterministic water pixels to calculate the shortest-path between every pair of nodes except for the stochastic edges found in the previous step. Since the path generated by A* connects neighbouring pixels, we smooth them by downsampling. Then, we can discard any unnecessary stochastic edges if they do not reduce the distance between a pair of nodes. For

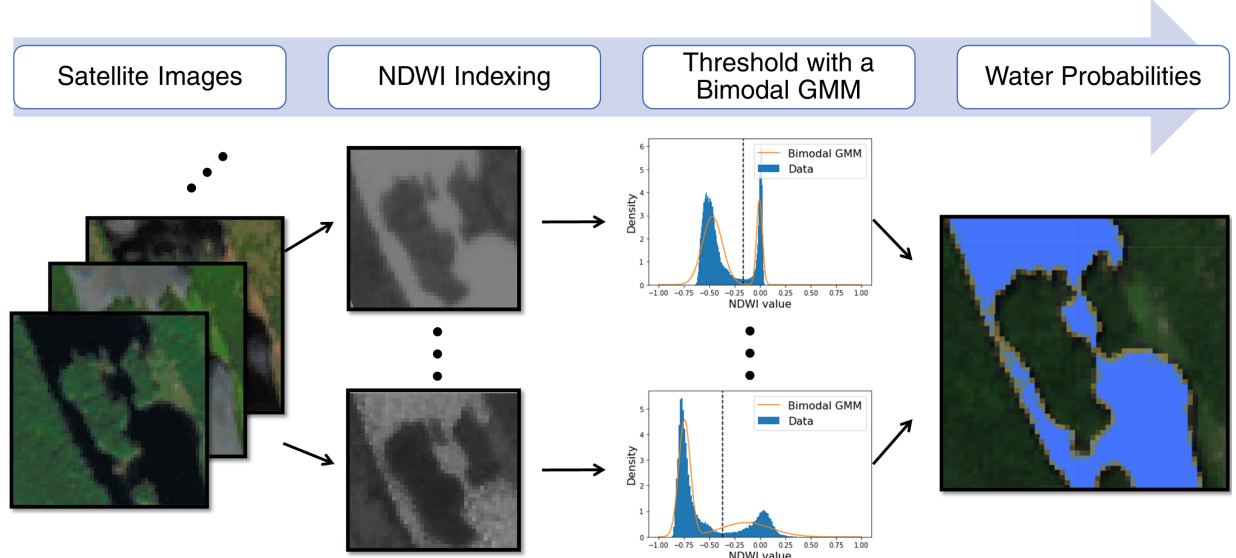


Figure 6: Overview of water-masking steps that calculate water probabilities from satellite images. Pixels with lower water probabilities are shaded more orange.

every stochastic edge, we loop over all pairs of nodes and check if setting the edge traversable would reduce the distance between the pair of nodes. Finally, we check if each deterministic edge is a windy edge and obtain the high-level graph used in PCCTP.

In summary, we estimate water probabilities from historical satellite images with adaptive NDWI indexing and build a stochastic graph connecting all sampling locations and pinch points. The resulting compact graph representing a PCCTP instance can be solved optimally with AO* heuristic search.

4 Simulations

In this chapter, we will verify the efficacy of our PCCTP planning framework in a large-scale simulation of mission-planning on real lakes.

4.1 Testing Dataset

We evaluate our mission-planning framework on Canadian lakes selected from the *CanVec Series Ontario* dataset (Natural Resources Canada, 2019). Published by *Natural Resources Canada*, this dataset contains geospatial data of over 1.1 million water bodies in Ontario. Considering a practical mission length, lakes are filtered such that their bounding boxes are 1-10 km by 1-10 km. Then, water masks of the resulting 5190 lakes are generated using *Sentinel-2* imagery across 30 days in June 2018-2022 (Drusch et al., 2012). We then detect any pinch points on the water masks and randomly sample five different sets of target nodes on each lake, each with a different number of targets. The starting locations are sampled near the shore to mimic real deployment conditions.

Furthermore, we generate high-level graphs and windy edges from the water mask. Graphs with no stochastic edges are removed as well as any instances with more than nine stochastic edges due to long run times. Ultimately, we evaluate our algorithm on 2217 graph instances, which come from 1052 unique lakes.

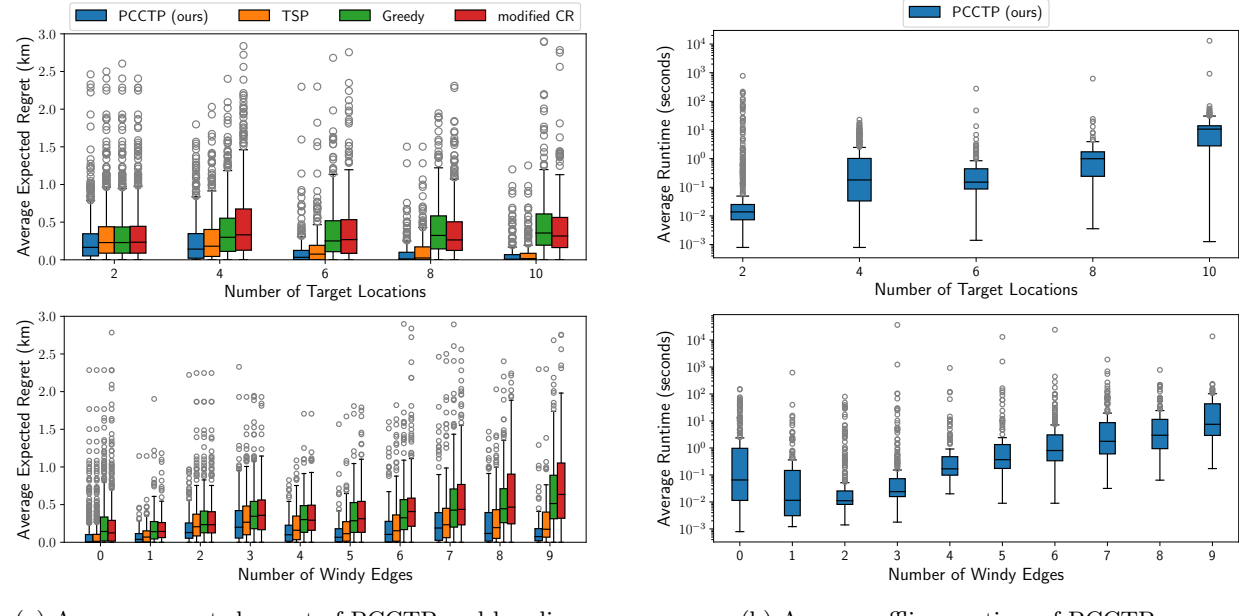


Figure 7: Results of PCCTP and baselines in simulation. When there are no windy edges, all stochastic edges are pinch points. We only show the runtime of PCCTP because all the baselines are online methods.

4.2 Baseline Planning Algorithms

The simplest baseline is an online greedy algorithm that always goes to the nearest unvisited target node assuming all ambiguous edges are traversable. For a graph with k stochastic edges, we simulate all 2^k possible worlds, each with a different traversability permutation, and evaluate our greedy actor on each one. The greedy actor recomputes a plan at every step and queries the simulator if it encounters a stochastic edge to disambiguate it. Also, it checks the reachability of every target node upon discovering an untraversable edge and gives up on any unreachable targets.

A more sophisticated baseline is the optimistic TSP algorithm. Instead of always going to the nearest target node, it computes the optimal tour to visit all remaining targets assuming all ambiguous edges are traversable. Similar to the greedy actor, TSP recomputes a tour at every step and may change its plan after encountering an untraversable edge. The expected cost is computed via a weighted sum on all 2^k possible worlds. In contrast to PCCTP, both baselines require onboard computation to update their optimistic plans, whereas PCCTP precomputes a single optimal policy that is executed online.

Lastly, we modify the CR algorithm, originally a method for CCTP (Liao & Huang, 2014), to solve PCCTP. CR precomputes a cyclic sequence to visit all target nodes using the Christofides algorithm (Christofides, 1976) and tries to visit all target nodes in multiple cycles while disambiguating stochastic edges. If a target node turns out to be unreachable, we allow CR to skip this node in its traversal sequence.

4.3 Results

Fig. 7a compares our algorithm against all baselines. To measure the performance across various graphs of different sizes, we use the average expected regret over all graphs. The expected regret of a policy π for one graph G is defined as

$$\mathbb{E}_w[\text{Regret}(\pi)] = \sum_w [p(w)(\phi(\pi, w) - \phi(\pi^p, w))],$$

where π^p is a privileged planner with knowledge of the states of all stochastic edges, ϕ is the cost functional, and w is a possible world of the graph. PCCTP precomputes the optimal policy in about 50 seconds on average in our evaluation, and there is no additional cost online. Compared to the strongest baseline (TSP), our algorithm saves the robot about 1%(50m) of travel distance on average and 15%(1.8km) in the extreme case. Although the improvement is marginal on average, our planner can still be beneficial in edge cases (e.g., high blocking probability, long stochastic edges). The performance of PCCTP may be further enhanced if the estimated blocking probabilities of the stochastic edges are refined based on historical data.

We also find that the performance gap between our algorithms and baselines becomes more significant with more windy edges. In fact, if the only type of stochastic edges in our graph is pinch points (i.e., the number of windy edges is 0), the performance gap is almost negligible between PCCTP and the optimistic TSP baseline. The main reason is that most pinch points only reduce the total trip distance by hundreds of meters on a possible world. Pinch points are most likely to be found either on the edges of a lake or as the only water link connecting two water bodies. In the first case, these pinch points are unlikely to be a big shortcut. As for the latter case, if the pinch point is the only path connecting the starting location to a target node, disambiguating this edge has to be part of the policy. On the other hand, windy edges passing through the centre of a lake are often longer, and the gap between the optimal and suboptimal policy is much more significant.

The worst-case complexity of our optimal search algorithm is $O(2^k)$ with respect to the number of stochastic edges k . The median runtime of our algorithm, implemented in Python, is less than one second, and 99% of the instances run under 3 minutes. However, in rare cases with eight or ten nodes, PCCTP can take up to ten hours using our unoptimized implementation. Note that the runtime can be considerably improved when our implementation is rewritten in a more efficient language, such as C++. More importantly, we argue that this one-time cost can occur offline before deploying the robot into a water-sampling mission. Although the worst-case runtime of the AO* algorithm can increase exponentially as the graph increases

in size, the number of target locations in each graph cannot grow infinitely for real-world water-sampling missions. Hence, the runtime of PCCTP is not a concern for practical applications.

5 Autonomous Navigation System

This section will explain our local navigation framework in detail and how the robot can execute the mission-level policy and safely follow its planned trajectory.

5.1 Stochastic Edge Disambiguation

One crucial aspect required for fully autonomous policy execution is the capacity to disambiguate stochastic edges. Our approach is to build a robust autonomy framework (Fig. 8) that relies less on lower-level components such as perception and local planning to execute a policy successfully. In more general terms, the mission planner precomputes the navigation policies from satellite images given user-designated sampling locations. During a mission, the robot will try to follow the global path published by the policy. Sensor inputs from a stereo camera and sonars are processed and filtered via a local occupancy-grid mapper. The local planner then tries to find a path in the local frame that tracks the global plan and avoids any obstacles detected close to the future path of the robot. When the robot is disambiguating a stochastic edge, the policy executor will independently decide the edge’s traversability based on the GPS location of the robot and a timer. A stochastic edge is deemed traversable if the robot reaches the endpoint of the prescribed path of this edge within the established time limit. If it fails to do so, the edge is deemed untraversable. There is no explicit traversability check on an ambiguous stochastic edge, such as a classifier or a local map. The timer allows us to address complications we cannot directly sense, such as heavy prevailing winds or issues with the local planner. Following this, the executor branches into different policy cases depending on the outcome of the disambiguation.

5.2 Terrain Assessment with Stereo Camera

An experienced human paddler or sailor can easily estimate traversability in a lake by visually distinguishing water from untraversable terrains, obstacles, or any dynamic objects. We use semantic information from RGB video streams and neural stereo disparity maps to estimate traversable waters in front of the robot and identify obstacles. We learn a water segmentation network and bundle it with a temporal filter to estimate the waterline in image space and remove outliers. The estimated waterline is then projected to 3D using the disparity map and used to update the occupancy grid. We provide more details in the following sections.

5.2.1 Water Segmentation Network

A robust neural network relies on a large and diverse dataset. The characteristics of water’s appearance exhibit considerable variation contingent on factors such as wind, reflections, and ambient brightness. Yet, the stereo camera falters in difficult lighting conditions due to the lack of dynamic range, culminating in inadequately exposed images and the emergence of artifacts such as shadows, lens flare, and noises. To navigate this challenge, applying data augmentation techniques such as colour-jittering and CutMix (Yun et al., 2019) during training greatly enhances out-of-distribution performance, yielding superior generalization in challenging weather conditions as in Fig. 9. Essentially, regions of one training image are cut and overlaid onto another, as demonstrated in Fig. 10 to encourage the model to learn more diverse and challenging features while also expanding our limited dataset.

Another problem arises as manual annotation of thousands of images is impractical due to its labour and time intensity. Thus, since semantic segmentation is a well-explored research area, we used a pretrained SAM (Segment Anything Model) to automate the process of creating ground-truth labels (Kirillov et al., 2023).

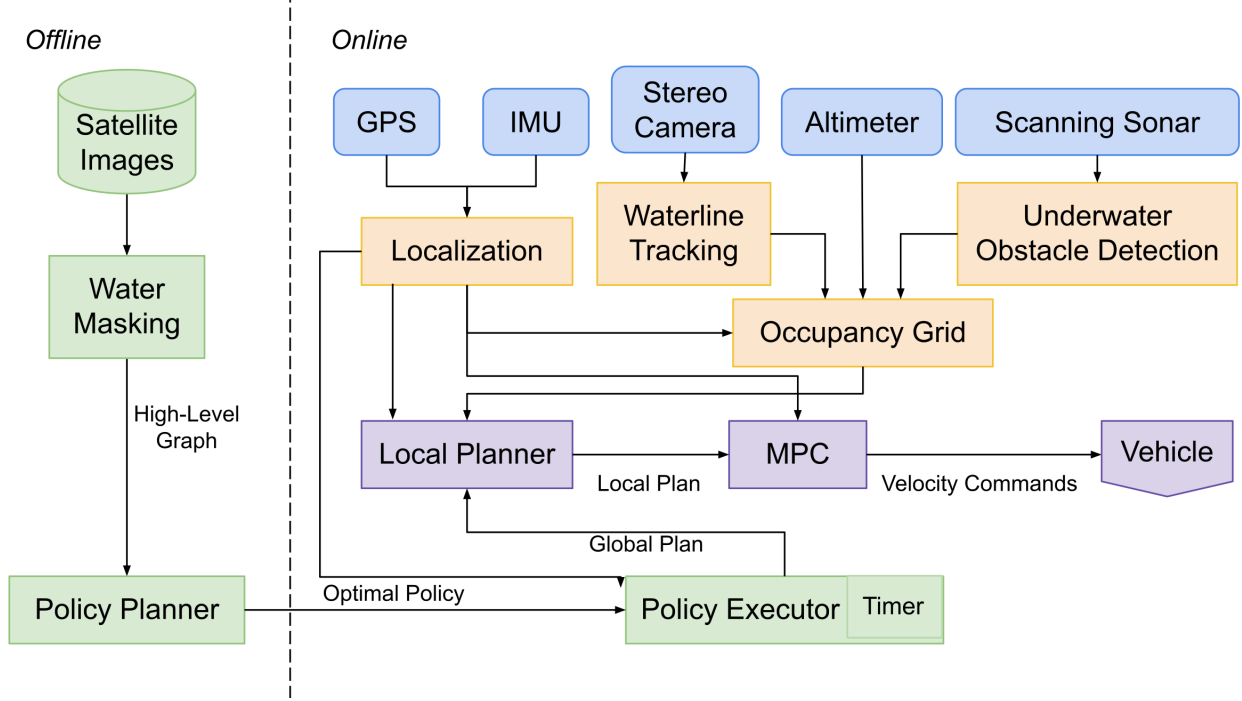


Figure 8: The autonomy modules of our navigation system. Global mission planners are coloured in green, sensors inputs are labelled in blue, localization and local mapping nodes are shaded in orange while planning and control nodes are in purple.

SAM will try to segment everything beyond just water, outputting numerous masks of different irrelevant items. While it is not yet capable of classifying labelled regions, because water normally occupies the lower half of the frame and is commonly characterized by substantial area and continuity, we can apply a heuristic that heavily favours these features, scoring regions to distinguish water mask m_{water} from other masks with very high accuracy:

$$m_{\text{water}} = \max_i \left[\frac{A(m_i)}{d(m_i) + 1} \right],$$

where m_i denotes the mask of class i from SAM, A computes the total number of pixels a mask occupies, and d represents the vertical distance, in pixels, of the masked area's centroid from the image's bottom. Then, false positives within the identified mask will be filtered out. With manual checking, we found that this simple approach successfully labelled the entirety of our dataset without failure. An example of this process is shown in Fig. 11. Finally, we have a binary mask ready to be fed into training.



(a) Sub-Optimal Exposure



(b) Reflections in Still Water

Figure 9: Examples of challenging conditions for semantic segmentation and disparity mapping.

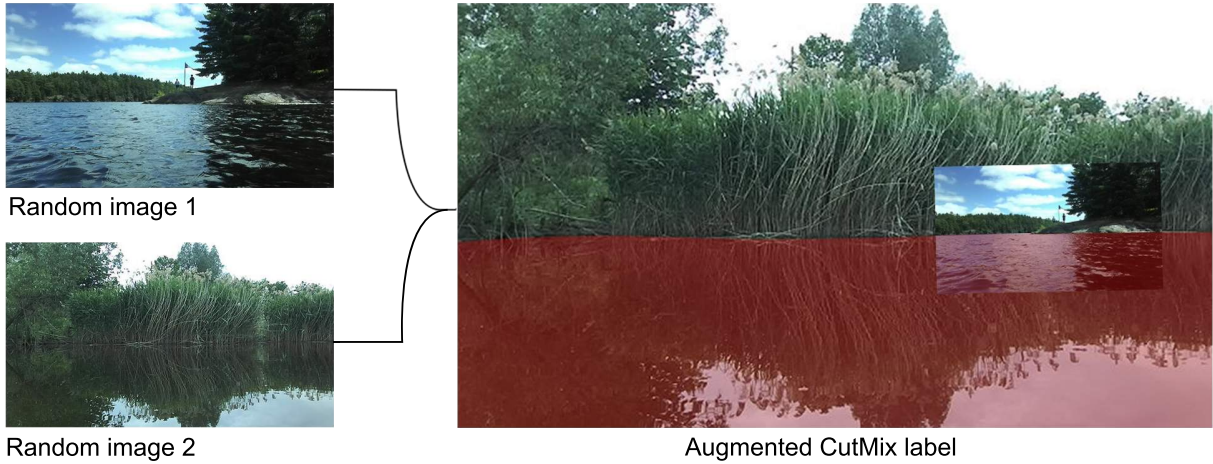


Figure 10: Example of CutMix augmented training data. A second image with a random exposure multiplier is randomly resized and placed on top of the original image. The red region highlights the pixels that are labelled as water.

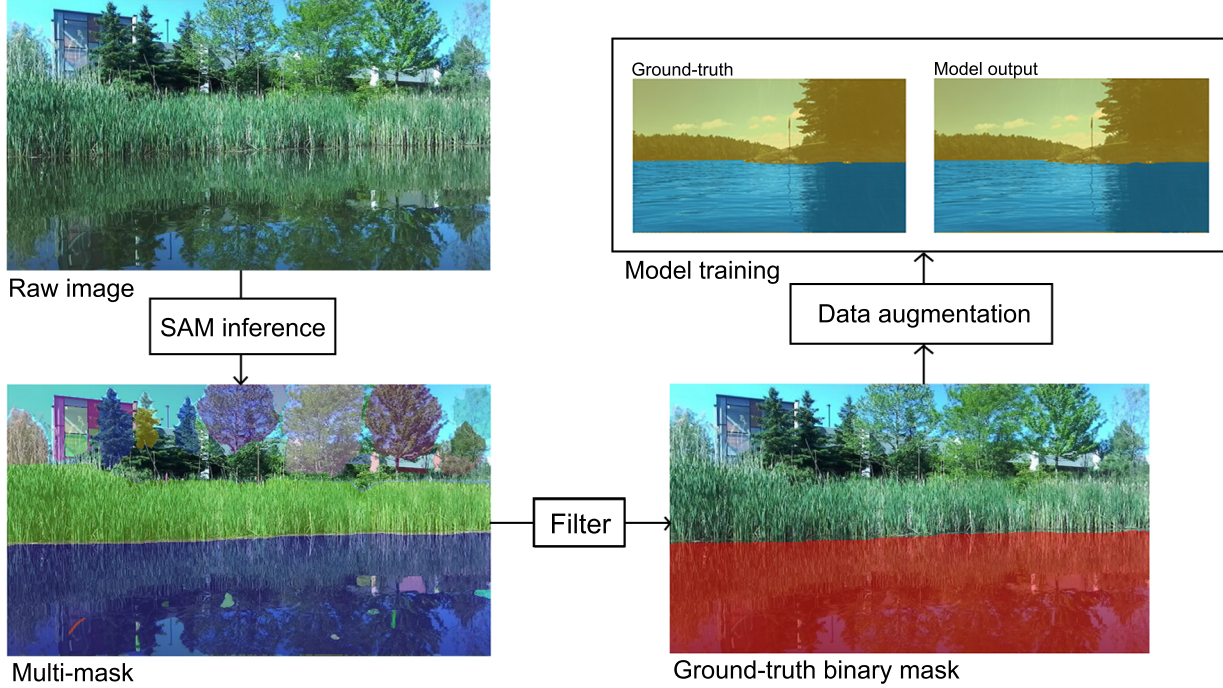


Figure 11: The steps in the automatic process of generating ground-truth labels. Each distinct colour overlay represents a different object as segmented by SAM. The red region is the final ground-truth water mask after heuristic filtration.

Our model architecture and pretrained weights are adopted from the eWaSR maritime obstacle detection network based on the ResNet-18 backbone (Teršek et al., 2023). From previous field tests in Nine Mile Lake and a stormwater management pond at the University of Toronto, we gathered around 4,000 images to serve as our training dataset and 200 for testing. In addition, 10 more labels are generated randomly using CutMix during training for every original labelled image. In the end, we are left with a lightweight



Figure 12: Example images from our test set. Diverse and challenging scenarios were hand-picked to better assess model capabilities.

yet powerful neural network that outputs binary masks that accurately and consistently segment water, achieving a mIoU of 0.992 with respect to ground truth on the held-out test set of 200 images (Fig. 12).

5.2.2 Waterline Estimation and Tracking

There are several issues associated with the direct use of raw segmentation masks produced by a neural network. Firstly, the 2D, per-pixel water labels are not inherently suited for determining traversability before the robot. Secondly, depth estimations derived from the stereo camera can be severely distorted due to unfavourable conditions such as sun glare or tranquil water reflections. Lastly, both the neural segmentation masks and depth maps can exhibit noise and inconsistency over successive timestamps. These issues necessitate that we avoid combining segmentation masks directly with depth maps to ascertain the existence of a 3D water surface. Instead, we filter the segmentation masks both spatially and temporally to approximate a waterline in 2D image space, then project this line into 3D space. This projected line then forms the basis for traversability estimates in 3D based on stereo data.

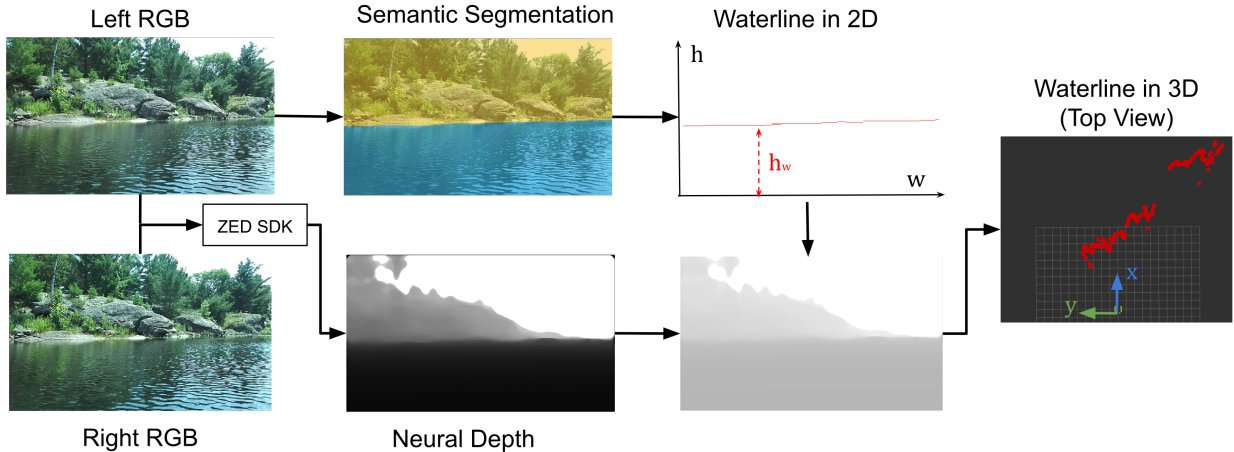


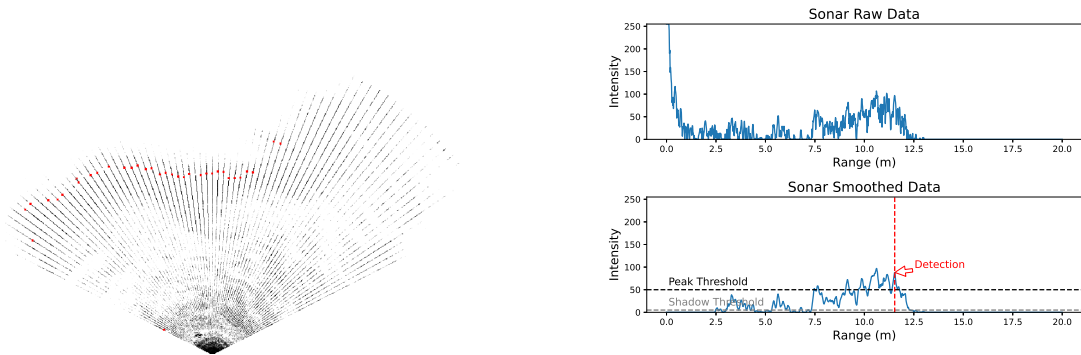
Figure 13: The stereo-based waterline estimation pipeline. Red dots indicate the detected waterline in the image plane and in 3D.

We approximate the 2D waterline as a vector comprising n elements, where n represents the image's width. Each element serves to indicate the waterline's position for that column. The fundamental premise here is that each column contains a clear division between the water and everything else – the sky, trees, people, shoreline buildings, and other dynamic obstacles. Thus, we can presume that only the pixels below the waterline are navigable, while those above are impassable. This model works well because water surfaces are typically horizontal when viewed from the first-person perspective of the ASV. Therefore, for the purpose of evaluating the robot's forward navigation, we can safely disregard any water pixels located behind in 3D, or higher than in the image space, the defined waterline. The position of the waterline on every column is identified by scanning upwards from the column's bottom until a non-water region is detected using a small moving window. If s is the window size, the separation point is the first pixel from the bottom such that the next s pixels above are all non-water. Usually, the window size is five.

Our filtering process consists of two stages: spatial filtering based on RANSAC (Fischler & Bolles, 1981) and employing a Kalman filter subsequently for temporal tracking of the waterline. We design the spatial filtering step to smooth the waterline and remove spatial outliers; to this end, we employ nearest-neighbour interpolation to fit the random samples in each iteration. RANSAC uses the squared loss function to compare the interpolated waterline and the raw waterline. Then, we apply a linear Kalman filter with outlier rejection to track each individual element (column) of the waterline temporally. The Kalman filter uses RANSAC-filtered waterline as observations and maintains an estimated waterline as the state. Both the state transition matrix and the observation matrix are identities. We use a chi-squared test to discard outliers, which compares the normalized innovation squared to a predetermined threshold. Using both filters, we can eliminate noises in the segmentation mask and mitigate any temporal oscillation or abrupt changes in the predicted water segmentation masks.

5.3 Obstacle Detection with Sonar

Sonar is commonly used as a sensor in maritime applications for both ships and submarines. A specific type, the Blue Robotics Ping360 mechanical scanning sonar, serves as our primary sensing module underwater. It is mounted underwater and operates by emitting an acoustic beam within a forward-facing fan-shaped cone. This beam has a consistent width (1°) and height (20°). The sonar then records the echoes reflected by objects, with the reflection strength relating directly to the target's density. By measuring the return time and factoring in the speed of sound in water, the range of these echoes can be determined. The sonar's transducer can also be rotated to control the horizontal angle of the acoustic beam. Configured to scan a 120° fan-shaped cone ahead of the boat, the sonar can complete these scans up to a range of 20m in approximately 3.5 seconds. Additionally, we also have a Ping1D Sonar Echosounder from Blue Robotics that measures water depth. The echosounder is mounted underwater and is bottom-facing. Each sonar scan



(a) Sonar Scan Bird's Eye View. Detections are red.

(b) A Single Sonar Scan and its detection

Figure 14: A sonar scan and obstacle detection result. The scan is taken from the same scene and timestamp as in Fig. 13.

yields a one-dimensional vector that corresponds to the reflection's intensity along the preset range. If an obstacle impedes the path of the acoustic beam, it prevents the beam from passing beyond the obstruction, leading to an acoustic shadow. This phenomenon facilitates obstacle detection via sonar scanning.

Fig. 14a illustrates a typical sonar scan cycle that detects obstacles. A single sonar scan's raw and processed data with the resulting detected obstacle are shown in Fig. 14b. The process begins with the removal of noisy reflections within a close range ($<2.5\text{m}$) before smoothing the scan using a moving-average filter. Following this, all local maxima above a specific peak threshold (50) are detected. An obstacle is identified at the first local maxima, where the average intensity post-peak falls below the shadow threshold (5). Both these thresholds are determined empirically.

A post-processing filter removes detections that do not persist across a minimum of n scans (with $n = 2$ in our configuration). This is accomplished by calculating the cosine similarity between the current intensity vector and its predecessor. If an obstacle is consistently detected n times, and the cosine similarity across these successive intensity vectors exceeds 0.9, along with spatial proximity, this detected obstacle point is included. In other words, any detections occurring in isolation, either spatially or temporally, are excluded.

5.4 Sensor Fusion with Local Occupancy Grid

Upon receiving detections from sonar and stereo cameras, they are fused into a coherent local representation to facilitate local path planning and robot control. We utilize the classic occupancy map (Elfes, 1989) for our local mapping representation. The traversability of each cell is determined by naively summing the separately maintained log-odds ratios for sonar and camera. Our occupancy grid is $40\text{m} \times 40\text{m}$, with a cell resolution of $0.5\text{m} \times 0.5\text{m}$, its centre moving in sync with the robot's odometry updates. Waterline points, as detected by the stereo camera, are ray-traced in 3D back to the robot, thus lowering the occupied probability of cells within the ray-tracing range. Cells containing or adjacent to waterline points have their occupied

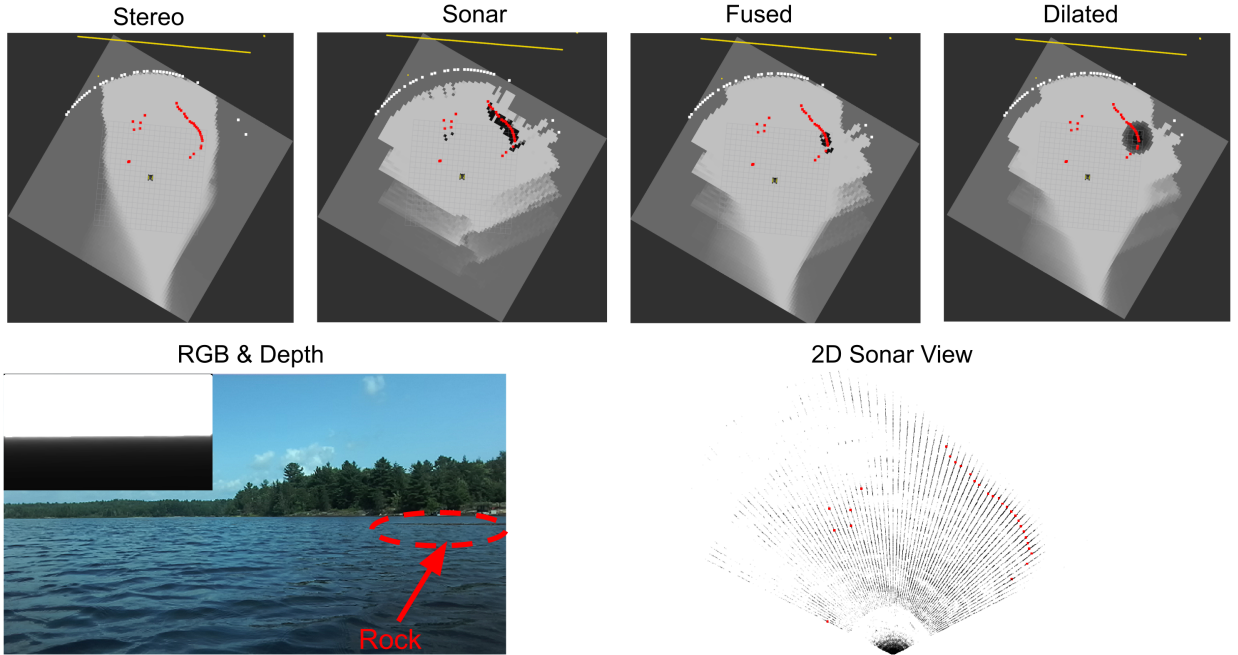


Figure 15: Example of sensor fusion with occupancy map before an extruding rock. **Yellow** line is the waterline estimated by stereo camera, **red** dots indicate underwater obstacles detected by the scanning sonar, and white dots mean that the sonar did not detect an obstacle at that angle.

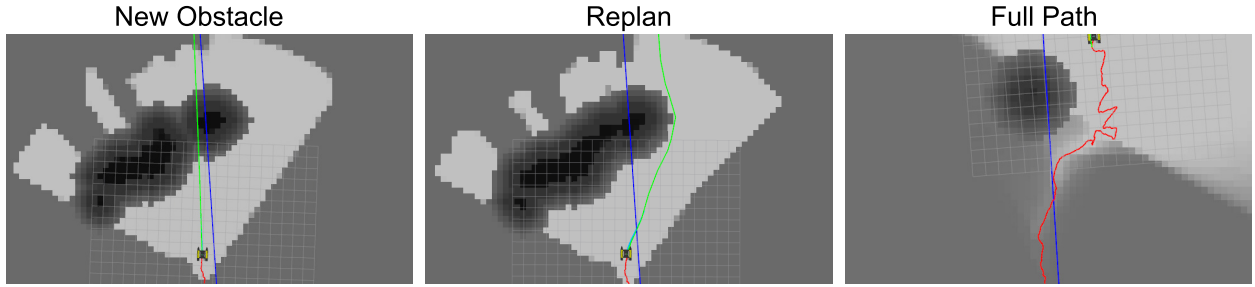


Figure 16: Example of the planner replanning around an obstacle and avoiding it. Blue line is the global plan (see Sec. 3.3 for details). Green is the current local plan planned using the local occupancy grid and tries to stay close to the global plan as much as possible (see Sec. 5.5). Red is the robot’s actual trajectory estimated by the GPS. The actual trajectory of the robot is jagged due to both noisy GPS signals and overaggressive control.

probabilities increased. However, points exceeding a set maximum range do not affect occupied probabilities beyond the maximum range due to the decreasing reliability of depth measurements with increasing range. The protocol for updating the log-odds ratios for sonar is similar. Each sonar scan is ray-traced to clear the occupancy grid and marks any cells containing or close to the obstacles. The log-odds ratios of existing cells are decayed with incoming measurement updates, enhancing the map’s adaptability to noisy localizations, false positives, and dynamic obstacles. Finally, we apply a median filter to the occupancy grid to smooth out and remove outliers.

A limitation of this system is that sonars and the stereo camera observe different sections of the environment. The sonar may detect underwater obstacles invisible to the camera and vice versa for surface-level objects. Fig. 15 provides an example where a shallow rock in the front-right of the ASV is detected by the sonar but missed by the stereo camera. Without ample ground-truth data on the marine environment, reconciling discrepancies between these sensors proves challenging. Traversability estimation, especially in shallow water, is also complicated due to the potential presence of underwater flora (e.g. Fig. 1c) or terrain. As a solution, we opt for the simplest fusion method: directly summing the log-odds ratio in each cell. Additionally, we adjust the occupancy grid dilation based on the echosounder’s water depth measurements, increasing the dilation radius when the ASV is in shallower water. The workflow of this strategy is shown in Fig. 15. While this strategy may only present a coarse traversability estimate, it still reliably detects the shoreline despite possible undetected smaller obstacles such as lily pads or weeds. The dilation adjustment employed in shallow water allows the ASV to navigate safely, avoiding prevalent aquatic plants near the shore.

5.5 Local Path Tracking and Control

The local planner and control we use are grounded in a modified version of Lateral BIT*, as proposed by Sehn et al. (2023). This optimal sampling-based planner, set within the VT&R (Furgale & Barfoot, 2010) framework, follows an arbitrary global path while veering minimally around obstacles. Lateral BIT* builds upon BIT* (Gammell et al., 2015) by implementing a weighted Euclidean edge metric in the curvilinear planning domain, with collision checks performed against the occupancy grid in the original Euclidean space. Samples are pre-seeded along the whole global path in the curvilinear coordinates before random sampling in a fixed-size sampling window around the robot. The planner operates backward from a singular goal node to the current robot location without selecting any intermediate waypoints. Lateral BIT* is also an anytime planner and can be adapted for dynamic replanning. Once an initial solution is found, an MPC tracking controller can track the solution path. The MPC optimizes the velocity commands in a short horizon to minimize the deviation from the planner solution while enforcing robot kinematic models and acceleration

constraints. Adopted from Sehn et al. (2023), the MPC solves the following least-squares problem:

$$\underset{\mathbf{T}, \mathbf{u}}{\operatorname{argmin}} J(\mathbf{T}, \mathbf{u}) = \sum_{k=1}^K \ln(\mathbf{T}_{\text{ref},k} \mathbf{T}_k^{-1})^{\vee^T} \mathbf{Q}_k \ln(\mathbf{T}_{\text{ref},k} \mathbf{T}_k^{-1})^{\vee} + \mathbf{u}_k^T \mathbf{R}_k \mathbf{u}_k$$

s.t.

$$\begin{aligned} \mathbf{T}_{k+1} &= \exp((\mathbf{P}^T \mathbf{u}_k)^{\wedge} h) \mathbf{T}_k, k = 1, 2, \dots, K \\ \mathbf{u}_{\min, k} &\leq \mathbf{u}_k \leq \mathbf{u}_{\max, k}, k = 1, 2, \dots, K \end{aligned}$$

where $\mathbf{T} \in SE(3)$ are poses and $\mathbf{u} = [v \ \omega]^T$ are velocities. The objective function minimizes the pose error between the reference trajectory $\mathbf{T}_{\text{ref},k}$ and the predicted trajectory \mathbf{T}_k while keeping the control effort \mathbf{u}_k minimum. The two constraints are the generalized kinematic constraint and actuation limits. We tune the cost matrices \mathbf{Q} and \mathbf{R} to balance the cost between different degrees of freedom. We refer readers to Sec. V of Sehn et al. (2023) for more details.

If a newly detected obstacle obstructs the current best solution path, the planner will truncate its planning tree from the obstacle to the robot, triggering a replan or rewire from the truncated tree to the robot's location. Fig. 16 shows an example from the field test where our robot detected obstacles and replanned its trajectory accordingly. Because the resolution of the satellite map is low (10m/cell), our global path could be blocked by large rocks and terrains, especially the pinch points. Hence, we adjust the maximum width and length of the sampling window and tune the parameters balancing lateral deviation and path length. If there are no viable paths locally within the sampling window and the planner cannot find a solution after 1 second, the controller will stop the ASV and stabilize it at its current location.

6 Real World Experiments

6.1 Robot

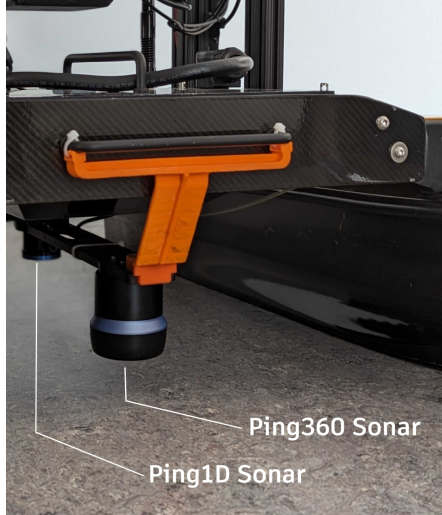
Our ASV platform, as depicted in Fig. 17, consists of a modified *Clearpath Heron* ASV equipped with a GPS, IMU, Zed2i stereo camera, Ping360 scanning sonar, and a Ping1d Sonar Echosounder Altimeter. The stereo camera is positioned in a forward-facing configuration and has a maximum depth range of 35 m. The Ping360 sonar is configured to perform a 20 m by 125° cone scan in front of the robot every 3.5 seconds, achieving a resolution of 1.8°. All computational tasks are handled by an Nvidia Jetson AGX Xavier and the onboard Intel Atom (E3950 @ 1.60GHz) PC on the Heron. A lithium-ion battery with an energy capacity of 88 WH powers the Jetson, stereo camera, and Ping360 sonar for approximately one hour, while a 417.6-Wh NiMH battery pack powers the motors and other electronic components for around two hours. A schematic of the electrical system is presented in Fig. 17c. The additional payloads carried by the ASV have a combined mass of roughly 9 kg. Although water samplers have not been integrated into our system, they can be easily fitted in the future. The maximum speed of our ASV is approximately 1.2 m/s. Additionally, we have a remote controller available for manual mode operation, which can be utilized for safety purposes if needed.

6.2 System Implementation Details

Our system's computational load is divided into offline and online processes (Figure 8). The online tasks are distributed between two onboard computers: the Atom PC and the Jetson. An Ethernet switch connects these computers, the sonar, and Heron's WiFi Radio. The GPS and IMU are connected to the Atom PC via USB, while the echo-sounder sonar and stereo cameras are connected to the Jetson via USB. The switch allows remote SSH access and data transfer between the Atom and the Jetson. We use the ROS framework (Quigley et al., 2009) for implementing our autonomy modules in C++ and Python. To synchronize time between the two machines, we employ Chrony for network time protocol setup. The Atom PC acts as the

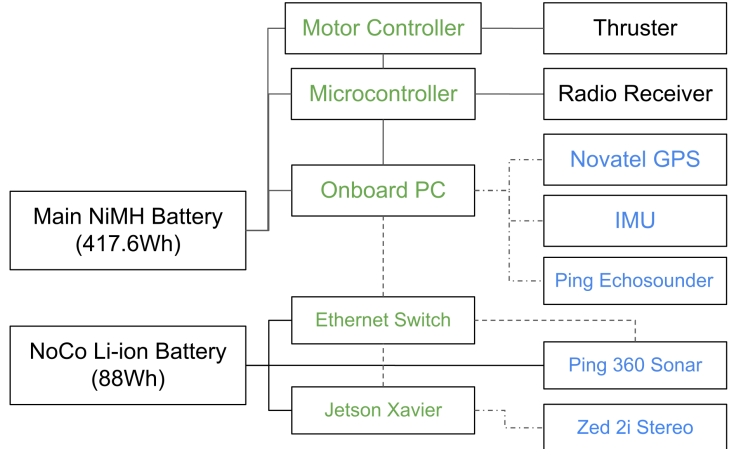


(a) Top View



(b) Bottom View

Ethernet ----- USB ----- Power ——



(c) Electrical Diagram

Figure 17: Our *Clearpath Heron* ASV for water-quality monitoring during a field test. The ASV has onboard sensors (GPS, IMU, underwater scanning sonar, stereo camera) and an Nvidia Jetson to process sensor measurements. Power and communication lines for our ASV are shown in (c).

ROS master, responsible for vehicle interface, localization, updating the occupancy grids, running the local planner, and MPC controller. The Jetson handles resource-intensive tasks such as depth map processing, semantic segmentation, sonar obstacle detection, and data logging. Additionally, we provide web visualization using a ROS node with a Node.js server, projecting the robot's global pose, trajectory, and plan onto a cached *OpenStreetMap* and water mask. We also provide a Rviz visualizer to display the occupancy grid and outputs of the local planner and MPC. During the mission, the web server publishes the robot's locations and states in real-time on a web page served on the local network, using pre-downloaded satellite maps. The web visualization and Rviz can be accessed in the field from a laptop connected to Heron's WiFi. Prior to the mission, we precompute the high-level graph and optimal policy, which are loaded onto the onboard PC. We periodically save the status of policy execution online, enabling easy policy reloading in case of a battery change during testing.

6.3 Testing Site

Our planning algorithm was evaluated at Nine Mile Lake in McDougall, Ontario, Canada. Detailed test sites and the three executed missions can be found in Fig. 18. The Lower Lake Mission in Fig. 18a repeats the field test from our prior work (Y. Huang et al., 2023), involving a 3.7 km mission with five sampling points, three of which are only reachable after navigating a stochastic edge. The stochastic edge at the bottom-left compels the ASV to maneuver through a thin opening amid substantial rocks not discernible in the *Sentinel-2* satellite images. Besides repeating the old experiment from our prior work, we added two additional missions in the lake’s upper areas. Also, to assess our local mapping and planning stack’s capabilities, an ablation mission was executed to see if the robot could safely navigate the stochastic edge at the bottom-left of the Lower Lake Mission. The policy in Upper Lake Mission (Short) was directly generated from the Fig. 3 water mask. In fact, the high-level graph in Fig. 3 and policy in Fig. 4 is a simplified toy version of our testing policy in the Upper Lake Mission (Short). We observed that our NovAtel GPS receiver’s reliability was impaired by large trees on the left stochastic edge in Fig. 18b. On the right stochastic edges of the same subfigure, shallow regions, lily pads, and weeds were numerous. Lastly, we extended this short mission to include three additional sampling sites and another stochastic edge at the lake’s farthest point. The expected length of this Upper Lake Mission (Long) in Fig. 18c is approximately 3.3km.

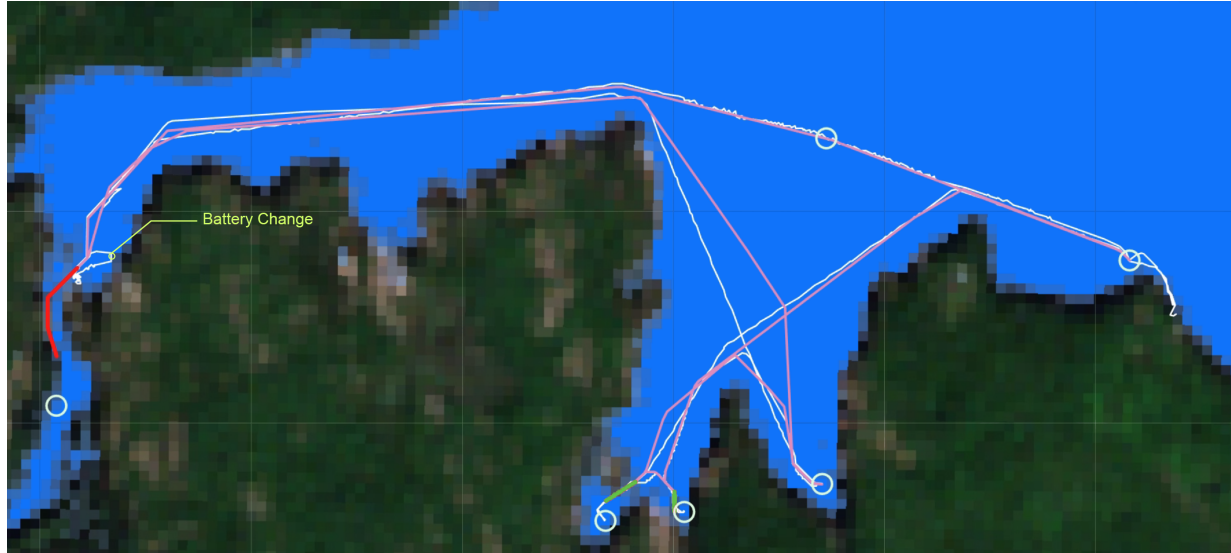
6.4 Results of Mission Planner

The aim of our field experiments is to test if our autonomy stack can successfully execute a global mission policy correctly and fully autonomously, without any manual interventions. Results are summarized in Table 1 and we provide the overview and analysis of our results below.

Table 1: Summary of the results of our tests for different policies, including any interventions due to algorithmic failure (excluding battery changes).

Mission	Sensors Used	Node Visited	Interventions
Lower Lake Mission	Sonar + Camera	4/5	Once
Lower Lake Mission	Camera Only	4/5	None
Upper Lake Mission (Short)	Sonar + Camera	1/1	None
Upper Lake Mission (Short)	Sonar + Camera	1/1	None
Upper Lake Mission (Short) (Left Edge Blocked)	Sonar + Camera	1/1	None
Upper Lake Mission (Short) (Left Edge Blocked)	Sonar + Camera	0/1	None
Upper Lake Mission (Long)	Sonar + Camera	5/5	Once

Lower Lake Mission We undertook the lower lake mission twice - first, using both sonar and camera, and second, using only the camera. The ASV successfully reached 4/5 targeted locations during both trials, with the exception of the bottom-left location. This was due to the ASV’s inability to autonomously navigate through large rocks within the designated time frame. When contrasted with prior experiments noted in Y. Huang et al. (2023), our trials showed marked improvement, with only a single manual intervention required due to algorithmic failure during the first run, and none during the second. The intervention was necessitated by the ASV’s collision with a tree trunk (the one in Fig. 1b) it failed to identify, resulting in manual maneuvering to remove the obstruction. In both trials, the policy executor deemed the bottom-left stochastic edge untraversable because the local planner did not find a path through large rocks within the time limit. The ASV was then safely directed back to the last sampling location and starting location. Moreover, through these trials, we noted a significant improvement in the stability of our navigational autonomy compared to the same field test last year. The inclusion of a new semantic segmentation network for the stereo camera allowed the ASV to navigate confidently even in conditions of high sunlight glare or calm water. Sonar detection capabilities facilitated the identification and avoidance of underwater rocks by the local planner. Through the incorporation of a Model Predictive Control (MPC) tracking controller, the reliance on GPS velocity estimates was removed. Lastly, the decision to use an 88Wh battery on the



(a) Lower Lake Mission



(b) Upper Lake Mission (Short)

(c) Upper Lake Mission (Long)

Figure 18: Representative examples of global plans and trajectories traversed during field experiments.

ASV markedly improved the Jetson’s battery life, thereby negating the need for battery changes during each mission. In Table 2, we show that the Jetson and onboard PC are very power-hungry during one of the testing trials. A microcontroller inside our ASV measures the power of the onboard PC, and we use the `jetson-stats` tool to log the power of the Jetson. Although the measurement is anecdotal and the exact power

Table 2: Usage and power consumption of our compute devices during a Lower Lake Mission.

Device	Heron CPU	Jetson CPU	Jetson GPU
Usage(%)	75.2	61.6	89.3
Power(W)	9.2	19.3 (Combined)	

consumption can depend on other factors, such as the state of the battery and operating temperatures, the 88WH battery powering the Jetson can certainly last through a two-hour-long experiment.

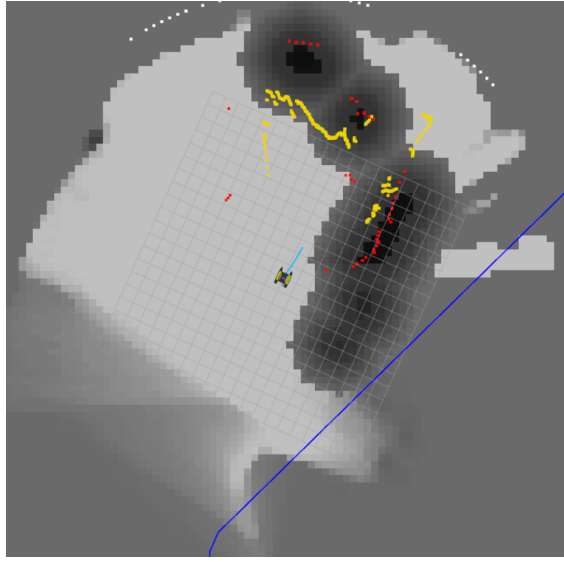
Upper Lake Mission (Short) We performed four tests of this policy on the upper lake to determine if our robot could execute different policy branches and navigate both sides of the central island, which were visibly passable based on aerial observations. The criteria for success entailed either a safe traversal through the stochastic edges on either side within the assigned time limit or a safe return to the start point without collisions. We initially executed the policy twice as it was. The policy guided the ASV to navigate and return along the left stochastic edge, which had a lower expected cost than the right edge. For the following two trials, we artificially executed a different branch of the policy by setting an early timeout, thereby blocking the left edge and compelling the ASV to navigate the right edge. The ASV executed the mission-level policy fully autonomously throughout all four trials, except for a battery change. Navigating the left side proved straightforward without any intervention, despite occasional GPS signal disruptions. On the right side, the ASV reached the target area once but timed out on the second trial. Despite the need for a battery change during one trial, no collisions occurred during any test. Importantly, we considered a trial a success despite the ASV not reaching the designated target if the overall policy was autonomously executed.

Upper Lake Mission (Long) We expanded the previous policy to a more extensive mission, covering a larger area of Nine Mile Lake’s upper parts with the same starting point as the shorter mission. First, the boat navigated the stochastic edges on the island’s left side to reach the sample point, and it returned using the same path. Despite this, significantly deteriorated GPS signals were observed at the edge’s end, preventing the mission-level policy executor from detecting the completion of the edge traversal due to GPS solution noise. Consequently, a manual restart of the policy executor was necessary. Thereafter, the ASV proceeded upwards to the next sample point before making a left turn to go through a shortcut pinch point, visiting two more sample points. Following a brief stop for battery replacement, the ASV completed the remaining mission. In evaluation, our local perception pipeline performed commendably in this area despite never previously collecting data here. Particularly, the synergy of sonar obstacle detection and stereo camera’s semantic waterline estimation showed high reliability in close-range shoreline and obstacle detection with very minimal false positives.

6.5 Isolated Testing of Local Planner

A main contribution of our current work is the new perception and local planner modules that can safely disambiguate stochastic edges and navigate safely and autonomously in obstacle and terrain-rich waterways without high-resolution prior maps. To verify this, we tested the local planner on a stochastic edge ten times with the exact same parameter, five times each in either direction. Success was demonstrated by either reaching the stochastic edge’s other endpoint within a set time frame or returning to the starting point upon timeout of the policy executor. Without intervention, the ASV accomplished this 70% of the time. However, in three instances, it collided with or became trapped by obstacles, such as rocks and a tree trunk.

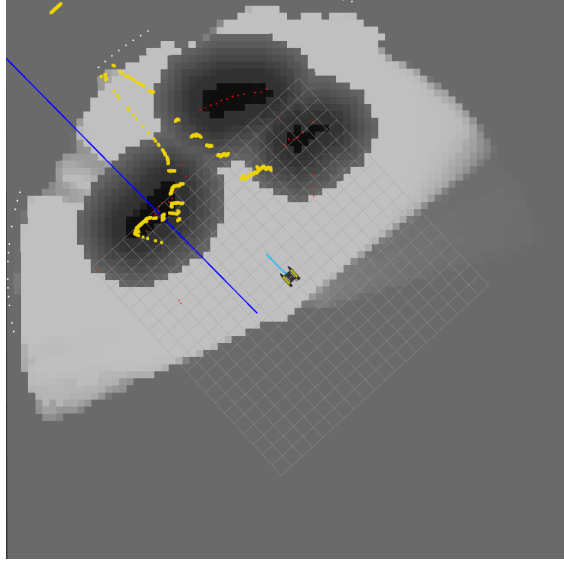
The global path extracted from the *Sentinel-2* Image was interrupted by a large rock, with only two narrow openings between the rocks, manually traversable, as demonstrated in Fig. 20 (b). One of the narrow openings is visible from the aerial view in Fig. 20 (d). Our ASV can detect these rocks; however, the over-aggressive dilation parameter obstructs the local planner from charting a path through the central passageway (see Fig. 19). Although marginally wider, the other opening exceeded the maximum corridor width of our local planner’s curvilinear space, being over 30m away from the nearest point on the global



(a) Occupancy Grid Map (ASV Start from South)



(b) Aerial View of the Scene in (a)



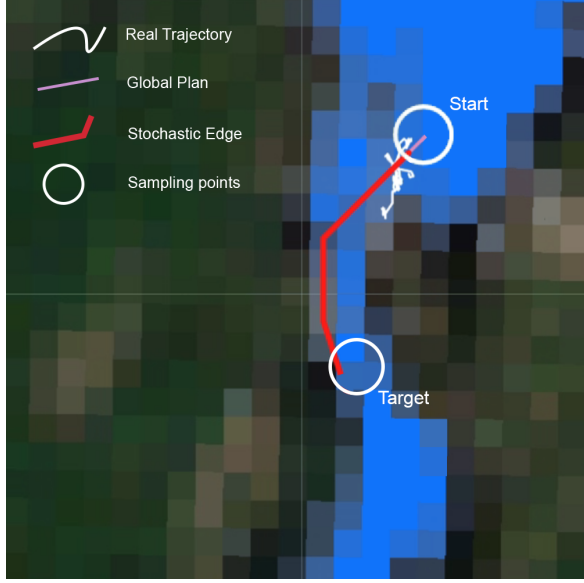
(c) Occupancy Grid Map (ASV Start from North)



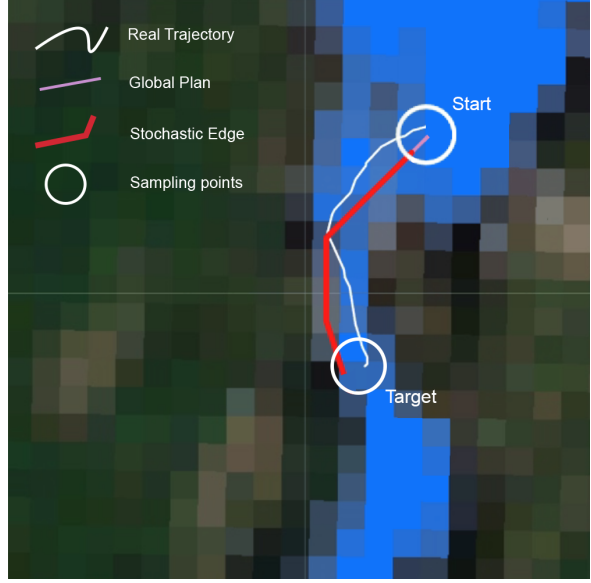
(d) Aerial View of the Scene in (c)

Figure 19: Comparison between the robot's occupancy grid maps and aerial image. **Yellow** dots are waterline estimated in 3D. **Red** dots are obstacles detected by sonar. Boat symbols are added to (b) and (d) for context. The global plan (**blue** line) is blocked by rocks, so the ASV needs to detour through the narrow opening. However, the passage is blocked on the occupancy grid due to our inaccurate detection, localization, and excessive dilation.

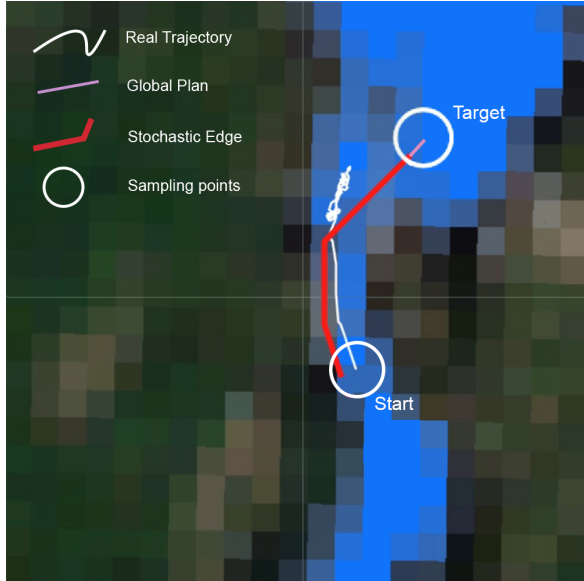
path. Relying exclusively on GPS/IMU for location and a local occupancy grid focused around the ASV poses considerable challenges in this terrain, due to imprecision in localizing obstacles relative to the robot and issues controlling tight turns and precise path tracking, escalating the collision risk in confined spaces. In order to mitigate noise and path plan conservatively, occupancy values were decayed over time, and substantial dilation was applied around occupied cells. As such, the ASV would not construct and finetune a consistent local map but would instead overlook previously encountered obstacles. Consequently, the local planner oscillates between two temporarily obstacle-free paths in the occupancy grid, while the ASV stops and unsuccessfully searches for a traversable path locally until the timer limit is reached, as shown in Fig. 20 (a) and Fig. 20 (c).



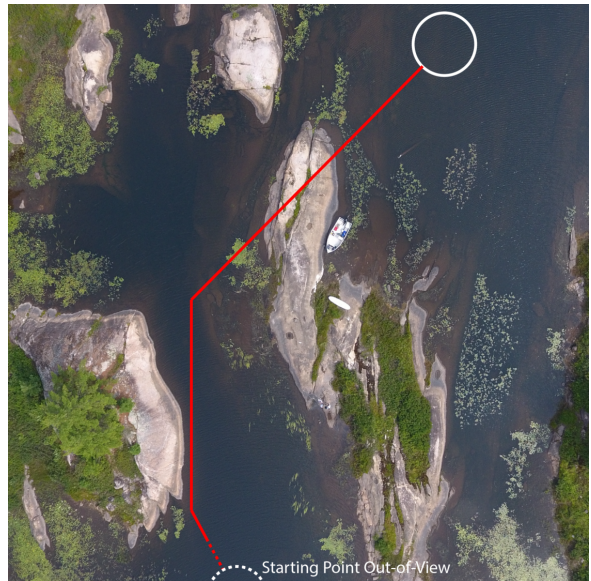
(a) Autonomous attempt (forward)



(b) Manual attempt (forward)



(c) Autonomous attempt (back)



(d) Aerial view (hand-sketched path from global plan)

Figure 20: Comparison of the global plan, manual traversal, and autonomous navigation through the stochastic edge. The global plan, calculated from coarse satellite images, is blocked by a rock. In (b), the ASV was able to pass the narrow opening under manual teleoperation. However, the ASV was unable to identify the opening in the local occupancy grid in autonomous mode (see. Fig. 19), so it searched for an opening in place until the time limit and returned to the start.

Another key reason for the low quality of the occupancy grid is the difficulty of fusing sonar and stereo camera measurements, especially at longer ranges. Since sensor fusion occurs solely within the occupancy map, both sensors need to detect an obstacle simultaneously at the same location in the map for accurate fusion. This can prove challenging due to a variety of reasons. For instance, depth measurements produced by the stereo camera tend to be noisier over a larger range. Our camera is not capable of detecting underwater obstacles detected by sonar. Additionally, our system lacks effective uncertainty measures for updating sonar and stereo observations within the occupancy map, especially when the two sources provide conflicting data. For example, the ASV simply did not detect the tree trunk. Thus, our sensor fusion mechanism proves effective

only over shorter ranges where the sonar and camera are more likely to align. If it is possible to extend the range of our perception modules, the ASV could formulate more optimized navigation paths, preventing collisions with obstacles such as rocks.

7 Lessons Learned

In this section, we outline insights garnered from our field tests, emphasizing successful design aspects related to field-tested ASV navigation systems and suggesting potential improvements for future iterations.

Timer Primarily, we found that using a timer to disambiguate stochastic edges was simple, robust, and practical. Integration of a timer within our ROS-based system was easy and could accommodate unexpected hindrances such as strong winds, making stochastic edges difficult to traverse. This allowed for uninterrupted policy execution even when the local planner failed to identify viable paths through a traversable stochastic edge. Essentially, the inclusion of a timer fostered independence between the execution of our mission-level policy and the selections of local planners, enabling the ASV to conduct water sampling missions irrespective of local planner errors.

Localization A critical limitation of our system lies in the absence of precise GPS localization. Our system necessitates a seamless integration of local mapping with broader satellite maps to facilitate accurate navigation in complex scenarios, such as those illustrated in Fig. 20. A GPS alternative, such as SLAM, would introduce redundancy, bolstering navigation robustness when GPS signals become compromised due to obstructions, interferences, or adverse weather conditions. Furthermore, minimizing localization noise could enhance speed and steering control, enabling the ASV to operate more swiftly and smoothly.

Occupancy Grid As demonstrated in the previous section, our occupancy grid map also struggles with sensor fusion - particularly over long ranges where sonar and stereo camera measurements can contradict. These inconsistencies necessitated the introduction of a time-decay factor and significant dilation around obstacles. As a result, we observed a ‘drunken sailor’ phenomenon, wherein the ASV constantly navigates within a confined space without any real progress. We think that semantic SLAM integration with the stereo camera could ameliorate local occupancy map issues. If SLAM can provide a locally consistent and metrically accurate map of higher quality, the decay factor in the occupancy grid becomes unnecessary and the planner will not oscillate. While SLAM is impractical in open water due to the absence of stationary features near the robot, it becomes viable in densely obstacle-populated scenes such as pinch points or shorelines. Localizing the robot against semantic-based local features could lead to more accurate localization and, furthermore, improve obstacle-relative pose estimation and traversability assessment. As we can store and grow the map as the robot explores unknown areas, the planner can also work with a static occupancy grid and avoid any oscillation. Furthermore, we also recommend better exploration strategies to build local maps and search for traversable paths rather than fixing the planning domain size around the precomputed global path from inaccurate satellite images.

As the map can be expanded when the robot explores unknown areas, the planner can work with a fixed occupancy grid to avoid oscillation. Additionally, more effective local map building and traversable path searching strategies might provide better solutions than confining the planning domain size around inaccurate satellite images’ precomputed global path.

Evasive Maneuvers Our system currently lacks evasive maneuvers. Despite collisions with obstacles, the robot could feasibly retreat and navigate back to unobstructed waters. However, our local planner often fails to detect forward obstacles, continuing to chart a forward path after collisions. Both the stereo camera and sonar have minimum range limitations, resulting in undetected proximate obstacles. We could introduce the timer mechanism to prompt evasive maneuvers. For instance, if the ASV remains stationary despite forward movement instructions from the planner and controller, it should back up and reset its local planner to circumnavigate the same area. While the ASV may struggle to self-extricate from a beach or shallow rock without human assistance, evasive maneuvers could facilitate the avoidance of obstacles such as tree trunks

or aquatic plants.

Sonar The incorporation of sonar in our system entails both advantages and drawbacks. Positively, it enabled the detection and circumvention of underwater obstacles, beyond the stereo camera’s capabilities. Conversely, the sonar’s slow scanning rate (3 seconds per scan) restricts it from being the solitary onboard perception sensor. Additionally, our heuristic-based obstacle detection method fails to recognize minor obstacles, such as lily pads or weeds. While the sonar effectively gauges obstacle distances from the ASV, it cannot determine the depth of underwater obstacles since it scans horizontally. This depth ambiguity complicates traversability estimation, which relies on exact water and underwater obstacle depth knowledge. Moreover, merging sonar with the stereo camera proves challenging due to their observing different world sections.

System Integration While our autonomy algorithms demonstrated commendable field performance, potential improvements from a system engineering standpoint remain. An immediate goal is enhancing our software’s efficiency to decrease computational load and power consumption on both the Atom PC and the Jetson. For instance, running semantic SLAM alongside the existing stack would require additional power and considerable software optimization to avoid straining our computers further. Aside from optimizing power use, improvements to efficiency, reliability, and usability could be advantageous, particularly for nontechnical users. Our Rviz and web interface user displays contain critical monitoring and debugging information but demand extensive navigation system familiarity. Our data logging pipeline consumes substantial storage space (about 1GB/min), imposing both storage and time cost burdens for copying and analysis. Booting up the GPS in the field was another challenge due to prolonged wait times for adequate satellite acquisition for autonomous navigation. In terms of future hardware, vegetation-proof boat hulls and propellers should be considered given the increased drag and potential damage to the propeller blades from aquatic plant interference. Furthermore, electronic connectors capable of withstanding transportation-induced vibrations and cables that shield connections from interference would enhance overall system robustness.

Field Logistics Our field logistics proved successful largely due to employing a motorboat, facilitating rapid transportation of the robot, personnel, and supplies to remote testing locations on the lake. During trials, staying in close proximity to the robot or flying a drone for tracking was straightforward using a motorboat. In case of forgotten crucial equipment, swift return trips to the base camp for recovery were possible. Our field tests, spanning three days, were completed as planned, despite limited time and battery life.

8 Conclusions

In conclusion, we have introduced a multi-sensor navigation system for Autonomous Surface Vehicles (ASVs) that uses satellite images to plan mission-level navigation policies offline. Our mission planner models the uncertainty in satellite images as stochastic edges, and formulates a Partial Covering Canadian Traveller Problem (PCCTP) on a high-level graph. We propose PCCTP-AO*, an optimal, informed-search-based method capable of finding a policy with the minimum expected cost. Our method has been evaluated in simulated graphs generated from real Canadian lakes, and results show that our optimal policy can save from 1%(50m) to 15%(1.8km) of travel distance. To deploy the policy for field operations, we construct a GPS-, vision-, and sonar-enabled navigation system to execute preplanned policies. Our local mapping modules combine a neurally estimated waterline from the stereo camera with underwater obstacles detected by a mechanically scanning sonar. The local motion planner then determines a path to avoid obstacles while still adhering to the global path from the precomputed policy. Through extensive field tests, we have demonstrated that our ASV navigation system can effectively execute the mission-level policy in the presence of unmapped obstacles with minimal intervention. Despite its simplicity, we found that the timer-based architecture can safely disambiguate stochastic edges and reliably complete km-scale missions. However, according to our ablation tests, traversability assessment and localization remain bottlenecks for local mapping and motion planning performance. We hope the lessons from this development process and the insights gained will foster advancements in future ASV systems.

Acknowledgments

We would like to acknowledge the Natural Sciences and Engineering Research Council of Canada (NSERC) for supporting this research.

References

Afrati, F., Cosmadakis, S., Papadimitriou, C. H., Papageorgiou, G., & Papakostantinou, N. (1986). The Complexity of the Travelling Repairman Problem. *RAIRO-Theoretical Informatics and Applications-Informatique Théorique et Applications*, 20(1), 79–87.

Aksakalli, V., Sahin, O. F., & Ari, I. (2016). An AO* Based Exact Algorithm for the Canadian Traveler Problem. *INFORMS Journal on Computing*, 28(1), 96–111.

Ang, Y.-T., Ng, W.-K., Chong, Y.-W., Wan, J., Chee, S.-Y., & Firth, L. B. (2022). An Autonomous Sailboat for Environment Monitoring. *2022 Thirteenth International Conference on Ubiquitous and Future Networks (ICUFN)*, 242–246.

Bai, S., Shan, T., Chen, F., Liu, L., & Englot, B. (2021). Information-Driven Path Planning. *Current Robotics Reports*, 2(2), 177–188.

Bellman, R. (1957). A Markovian Decision Process. *Journal of Mathematics and Mechanics*, 679–684.

Bovcon, B., Muhovič, J., Perš, J., & Kristan, M. (2019). The MaSTr1325 Dataset for Training Deep USV Obstacle Detection Models. *2019 IEEE/RSJ International Conference on Intelligent Robots and Systems (IROS)*.

Bovcon, B., Muhovič, J., Vranac, D., Mozetič, D., Perš, J., & Kristan, M. (2021). MODS – A USV-Oriented Object Detection and Obstacle Segmentation Benchmark.

Cao, H., Guo, Z., Wang, S., Cheng, H., & Zhan, C. (2020). Intelligent Wide-Area Water Quality Monitoring and Analysis System Exploiting Unmanned Surface Vehicles and Ensemble Learning. *Water*, 12(3), 681.

Chang, C. L., & Slagle, J. R. (1971). An Admissible and Optimal Algorithm for Searching AND/OR Graphs. *Artif. Intell.*, 2(2), 117–128.

Chang, H.-C., Hsu, Y.-L., Hung, S.-S., Ou, G.-R., Wu, J.-R., & Hsu, C. (2021). Autonomous Water Quality Monitoring and Water Surface Cleaning for Unmanned Surface Vehicle. *Sensors*, 21(4).

Chen, K., Liu, C., Chen, H., Zhang, H., Li, W., Zou, Z., & Shi, Z. (2023). RSPrompter: Learning to Prompt for Remote Sensing Instance Segmentation based on Visual Foundation Model.

Cheng, Y., Jiang, M., Zhu, J., & Liu, Y. (2021). Are We Ready for Unmanned Surface Vehicles in Inland Waterways? The USVInland Multisensor Dataset and Benchmark. *IEEE Robotics and Automation Letters*, 6(2), 3964–3970.

Christofides, N. (1976). Worst-Case Analysis of a New Heuristic for the Travelling Salesman Problem. *Operations Research Forum*, 3.

Dash, P., Moorhead, R. J., Herman, J., Beshah, W., Sankar, M. S., Moorhead, J., Chessler, G. D., Lowe, W., Simmerman, J., Turnage, G., Katkar, A. P., & Liles, J. P. (2021). Evaluation of Water Quality Data Collected using a Novel Autonomous Surface Vessel. *OCEANS 2021: San Diego – Porto*, 1–10.

Drusch, M., Del Bello, U., Carlier, S., Colin, O., Fernandez, V., Gascon, F., Hoersch, B., Isola, C., Laberinti, P., Martimort, P., Meygret, A., Spoto, F., Sy, O., Marchese, F., & Bargellini, P. (2012). Sentinel-2: ESA’s Optical High-Resolution Mission for GMES Operational Services [The Sentinel Missions - New Opportunities for Science]. *Remote Sensing of Environment*, 120, 25–36. <https://doi.org/https://doi.org/10.1016/j.rse.2011.11.026>

Dunbabin, M., & Marques, L. (2012). Robots for Environmental Monitoring: Significant Advancements and Applications. *IEEE Robot. Autom. Mag.*, 19(1), 24–39.

Elfes, A. (1989). Using Occupancy Grids for Mobile Robot Perception and Navigation. *Computer*, 22(6), 46–57.

Ester, M., Kriegel, H.-P., Sander, J., & Xu, X. (1996). A Density-Based Algorithm for Discovering Clusters in Large Spatial Databases with Noise. *Proceedings of the Second International Conference on Knowledge Discovery and Data Mining*, 226–231.

Ferguson, D., & Stentz, A. (2007). Field D*: An Interpolation-Based Path Planner and Replanner. *Robotics Research: Results of the 12th International Symposium ISRR*, 239–253.

Ferguson, D., Stentz, A., & Thrun, S. (2004, January). *Planning with Pinch Points* (tech. rep.). Carnegie-Mellon Univ Pittsburgh PA Robotics Inst.

Ferri, G., Manzi, A., Fornai, F., Ciuchi, F., & Laschi, C. (2015). The HydroNet ASV, a Small-Sized Autonomous Catamaran for Real-Time Monitoring of Water Quality: From Design to Missions at Sea. *IEEE J. Oceanic Eng.*, 40(3), 710–726.

Feyisa, G. L., Meilby, H., Fensholt, R., & Proud, S. R. (2014). Automated Water Extraction Index: A New Technique for Surface Water Mapping Using Landsat Imagery. *Remote Sens. Environ.*, 140, 23–35.

Fischler, M. A., & Bolles, R. C. (1981). Random Sample Consensus: A Paradigm for Model Fitting with Applications to Image Analysis and Automated Cartography. *Commun. ACM*, 24(6), 381–395. <https://doi.org/10.1145/358669.358692>

Furgale, P., & Barfoot, T. D. (2010). Visual Teach and Repeat for Long-Range Rover Autonomy. *Journal of Field Robotics*, 27(5), 534–560. <https://doi.org/10.1002/rob.20342>

Gammell, J. D., Srinivasa, S. S., & Barfoot, T. D. (2015). Batch Informed Trees (BIT*): Sampling-based Optimal Planning via the Heuristically Guided Search of Implicit Random Geometric Graphs. *2015 IEEE International Conference on Robotics and Automation (ICRA)*. <https://doi.org/10.1109/icra.2015.7139620>

Guo, H., & Barfoot, T. D. (2019). The Robust Canadian Traveler Problem Applied to Robot Routing. *2019 International Conference on Robotics and Automation (ICRA)*, 5523–5529.

Hart, P. E., Nilsson, N. J., & Raphael, B. (1968). A Formal Basis for the Heuristic Determination of Minimum Cost Paths. *IEEE transactions on Systems Science and Cybernetics*, 4(2), 100–107.

Heidarsson, H. K., & Sukhatme, G. S. (2011a). Obstacle Detection and Avoidance for an Autonomous Surface Vehicle using a Profiling Sonar. *2011 IEEE International Conference on Robotics and Automation*, 731–736.

Heidarsson, H. K., & Sukhatme, G. S. (2011b). Obstacle Detection from Overhead Imagery using Self-Supervised Learning for Autonomous Surface Vehicles. *2011 IEEE/RSJ International Conference on Intelligent Robots and Systems*, 3160–3165.

Huang, C., Chen, Y., Zhang, S., & Wu, J. (2018). Detecting, Extracting, and Monitoring Surface Water From Space Using Optical Sensors: A Review. *Rev. Geophys.*, 56(2), 333–360.

Huang, Y., Dugmag, H., Barfoot, T. D., & Shkurti, F. (2023). Stochastic Planning for ASV Navigation Using Satellite Images. *2023 IEEE International Conference on Robotics and Automation (ICRA)*. <https://doi.org/10.1109/icra48891.2023.10160894>

Ji, J., Khajepour, A., Melek, W. W., & Huang, Y. (2016). Path Planning and Tracking for Vehicle Collision Avoidance Based on Model Predictive Control with Multiconstraints. *IEEE Transactions on Vehicular Technology*, 66(2), 952–964.

Karaman, S., & Frazzoli, E. (2011). Sampling-Based Algorithms for Optimal Motion Planning. *The international journal of robotics research*, 30(7), 846–894.

Karoui, I., Quidu, I., & Legris, M. (2015). Automatic Sea-Surface Obstacle Detection and Tracking in Forward-Looking Sonar Image Sequences. *IEEE Trans. Geosci. Remote Sens.*, 53(8), 4661–4669.

Kirillov, A., Mintun, E., Ravi, N., Mao, H., Rolland, C., Gustafson, L., Xiao, T., Whitehead, S., Berg, A. C., Lo, W.-Y., Dollár, P., & Girshick, R. (2023). Segment Anything. *arXiv:2304.02643*.

Koenig, S., & Likhachev, M. (2002). D* Lite. *Eighteenth national conference on Artificial intelligence*, 476–483.

Laporte, G. (1992). The Traveling Salesman Problem: An Overview of Exact and Approximate Algorithms. *European Journal of Operational Research*, 59, 231–247.

Lee, S.-J., Roh, M.-I., Lee, H.-W., Ha, J.-S., & Woo, I.-G. (2018). Image-Based Ship Detection and Classification for Unmanned Surface Vehicle using Real-Time Object Detection Neural Networks. *The 28th International Ocean and Polar Engineering Conference*.

Li, J., & Sheng, Y. (2012). An Automated Scheme for Glacial Lake Dynamics Mapping using Landsat Imagery and Digital Elevation Models: a Case Study in the Himalayas. *Int. J. Remote Sens.*, 33(16), 5194–5213.

Liao, C.-S., & Huang, Y. (2014). The Covering Canadian Traveller Problem. *Theoretical Computer Science*, 530, 80–88. <https://doi.org/https://doi.org/10.1016/j.tcs.2014.02.026>

Maalouf, A., Jadhav, N., Jatavallabhula, K. M., Chahine, M., Vogt, D. M., Wood, R. J., Torralba, A., & Rus, D. (2023). Follow Anything: Open-set detection, tracking, and following in real-time. *arXiv preprint arXiv:2308.05737*.

Madeo, D., Pozzebon, A., Mocenni, C., & Bertoni, D. (2020). A Low-Cost Unmanned Surface Vehicle for Pervasive Water Quality Monitoring. *IEEE Trans. Instrum. Meas.*, *69*(4), 1433–1444.

MahmoudZadeh, S., Abbasi, A., Yazdani, A., Wang, H., & Liu, Y. (2022). Uninterrupted Path Planning System for Multi-USV Sampling Mission in a Cluttered Ocean Environment. *Ocean Eng.*, *254*, 111328.

Martelli, A., & Montanari, U. (1978). Optimizing Decision Trees Through Heuristically Guided Search. *Commun. ACM*, *21*, 1025–1039.

McFeeters, S. K. (1996). The Use of the Normalized Difference Water Index (NDWI) in the Delineation of Open Water Features. *International Journal of Remote Sensing*, *17*, 1425–1432.

Natural Resources Canada. (2019). Lakes, Rivers and Glaciers in Canada - CanVec Series - Hydrographic Features.

Noon, C. E., & Bean, J. C. (1993). An Efficient Transformation of the Generalized Traveling Salesman Problem. *INFOR Inf. Syst. Oper. Res.*, *31*(1), 39–44.

Odetti, A., Bruzzone, G., Altosole, M., Viviani, M., & Caccia, M. (2020). SWAMP, an Autonomous Surface Vehicle Expressly Designed for Extremely Shallow Waters. *Ocean Eng.*, *216*, 108205.

Papadimitriou, C. H., & Yannakakis, M. (1991). Shortest Paths Without a Map. *Theoretical Computer Science*, *84*(1), 127–150.

Pekel, J.-F., Cottam, A., Gorelick, N., & Belward, A. S. (2016). High-Resolution Mapping of Global Surface Water and its Long-Term Changes. *Nature*, *540*(7633), 418–422.

Perron, L., & Furnon, V. (2023, August 8). *Or-tools* (Version v9.7). <https://developers.google.com/optimization/>

Polychronopoulos, G. H., et al. (n.d.). Stochastic Shortest Path Problems with Recourse. *Networks*.

Qiao, D., Liu, G., Li, W., Lyu, T., & Zhang, J. (2022). Automated Full Scene Parsing for Marine ASVs using Monocular Vision. *J. Intell. Rob. Syst.*, *104*(2).

Quigley, M., Conley, K., Gerkey, B., Faust, J., Foote, T., Leibs, J., Wheeler, R., Ng, A. Y., et al. (2009). ROS: an Open-Source Robot Operating System. *ICRA workshop on open source software*, *3*(3.2), 5.

Sanchez-Ibanez, J. R., Perez-del-Pulgar, C. J., & Garcia-Cerezo, A. (2021). Path Planning for Autonomous Mobile Robots: A Review. *Sensors*, *21*(23), 7898.

Schiaretti, M., Chen, L., & Negenborn, R. R. (2017). Survey on Autonomous Surface Vessels: Part I - A New Detailed Definition of Autonomy Levels. *Computational Logistics*, 219–233.

Sehn, J., Collier, J., & Barfoot, T. D. (2023). Off the beaten track: Laterally weighted motion planning for local obstacle avoidance.

Shan, Y., Zheng, B., Chen, L., Chen, L., & Chen, D.-w. (2020). A Reinforcement Learning-Based Adaptive Path Tracking Approach for Autonomous Driving. *IEEE Transactions on Vehicular Technology*, *69*, 10581–10595.

Steccanella, L., Bloisi, D. D., Castellini, A., & Farinelli, A. (2020). Waterline and Obstacle Detection in Images from Low-Cost Autonomous Boats for Environmental Monitoring. *Rob. Auton. Syst.*, *124*, 103346.

Steccanella, L., Bloisi, D., Blum, J., & Farinelli, A. (2019). Deep Learning Waterline Detection for Low-Cost Autonomous Boats. *Intelligent Autonomous Systems* *15*, 613–625.

Tang, X., Pei, Z., Yin, S., Li, C., Wang, P., Wang, Y., & Wu, Z. (2020). Practical Design and Implementation of an Autonomous Surface Vessel Prototype: Navigation and Control. *International Journal of Advanced Robotic Systems*, *17*(3), 1729881420919949.

Teršek, M., Žust, L., & Kristan, M. (2023). Ewasr – an embedded-compute-ready maritime obstacle detection network.

Toth, P., & Vigo, D. (2002). *The Vehicle Routing Problem* (P. Toth & D. Vigo, Eds.). Society for Industrial; Applied Mathematics. <https://doi.org/10.1137/1.9780898718515>

Vasilj, J., Stančić, I., Grujić, T., & Musić, J. (2017). Design, development and testing of the modular unmanned surface vehicle platform for marine waste detection. *Journal of Multimedia Information System*, *4*(4), 195–204. <https://doi.org/10.9717/JMIS.2017.4.4.195>

Xu, H. (2006). Modification of Normalised Difference Water Index (NDWI) to Enhance Open Water Features in Remotely Sensed Imagery. *Int. J. Remote Sens.*, 27(14), 3025–3033.

Yang, J., Li, Y., Zhang, Q., & Ren, Y. (2019). Surface Vehicle Detection and Tracking with Deep Learning and Appearance Feature. *2019 5th International Conference on Control, Automation and Robotics (ICCAR)*, 276–280.

Yang, X., Zhao, S., Qin, X., Zhao, N., & Liang, L. (2017). Mapping of Urban Surface Water Bodies from Sentinel-2 MSI Imagery at 10 m Resolution via NDWI-Based Image Sharpening. *Remote Sensing*, 9(6), 596.

Yin, Y., Guo, Y., Deng, L., & Chai, B. (2022). Improved PSPNet-based Water Shoreline Detection in Complex Inland River Scenarios. *Complex & Intelligent Systems*.

Yun, S., Han, D., Oh, S. J., Chun, S., Choe, J., & Yoo, Y. (2019). CutMix: Regularization Strategy to Train Strong Classifiers with Localizable Features.

Zhou, R., Gao, Y., Wu, P., Zhao, X., Dou, W., Sun, C., Zhong, Y., & Wang, Y. (2022). Collision-Free Waterway Segmentation for Inland Unmanned Surface Vehicles. *IEEE Trans. Instrum. Meas.*, 71, 1–16.